White Rose Research Online

eprints@whiterose.ac.uk
https://eprints.whiterose.ac.uk
Universities of Leeds, Sheffield and York

Deposited via The University of Leeds.

White Rose Research Online URL for this paper:
https://eprints.whiterose.ac.uk/id/eprint/246749/

Version: Accepted Version

Article:
Sun, J., Huang, W., Liu, J. et al. (2026) Unveiling the Interfacial Strengthening Mechanism of the Epoxy Asphalt–Steel Slag System via Molecular Dynamics Simulation. Langmuir, 42 (36). pp. 26694-26712. ISSN: 0743-7463

https://doi.org/10.1021/acs.langmuir.6c03738

This is an author produced version of an article published in Langmuir, made available via the University of Leeds Research Outputs Policy under the terms of the Creative Commons Attribution License (CC-BY), which permits unrestricted use, distribution and reproduction in any medium, provided the original work is properly cited.

Reuse
This article is distributed under the terms of the Creative Commons Attribution (CC BY) licence. This licence allows you to distribute, remix, tweak, and build upon the work, even commercially, as long as you credit the authors for the original work. More information and the full terms of the licence here: https://creativecommons.org/licenses/

Takedown
If you consider content in White Rose Research Online to be in breach of UK law, please notify us by emailing eprints@whiterose.ac.uk including the URL of the record and the reason for the withdrawal request.

UNIVERSITY OF LEEDS
University of Sheffield
UNIVERSITY of York

Unveiling the interfacial strengthening mechanism of the epoxy asphalt-steel slag system via molecular dynamics simulation

Jia Sun [a], Wei Huang [b], Jiazheng Liu [c], Bohao Zhang [a], Qianyun Guo [a], Zhihan Zhang [a], Yuhao Du [a], Ali Rahman [d], Yue Huang [e], Sang Luo [b, *]

[a] *School of Transportation, Southeast University, Nanjing, Jiangsu, 211189, P. R. China*

[b] *Intelligent Transportation System Research Center, Southeast University, Nanjing, Jiangsu, 211189, P. R. China*

[c] *Jiangsu Provincial Transportation Engineering Construction Bureau, Nanjing, Jiangsu, 210004, P. R. China*

[d] *School of Civil Engineering, University of Leeds, Leeds, LS2 9LG, UK*

[e] *Institute for Transport Studies, University of Leeds, Leeds, LS2 9JT, UK*

***Corresponding author:**

Name: Sang Luo

Address: Intelligent Transportation System Research Center, Southeast University, Nanjing, Jiangsu, 211189, P. R. China

E-mail: 101011363@seu.edu.cn

Abstract: Steel slag (SS), a widely produced industrial solid waste, presents a sustainable alternative to natural pavement aggregates. However, its broader utilization is often restricted by moisture-induced interfacial debonding. To elucidate the microscopic interfacial mechanisms of epoxy asphalt (EA) in SS systems, this study integrates molecular dynamics simulations with laboratory experimental validation. Representative SS mineral crystal models were constructed to build atomistic EA–SS interfaces, facilitating the systematic investigation of adhesion, moisture stability, and molecular diffusion. Natural basalt and limestone aggregates were also examined for comparison. Results indicate that epoxy modification significantly improves interfacial thermodynamic stability. It shifts the primary adhesion mechanism from van der Waals forces to electrostatic interactions, particularly at the Ca^{2+}-rich surfaces characteristic of SS. Under moisture intrusion, the energy ratio (*ER*) of EA systems exhibits a notable increase. Specifically, the *ER* of the EA40 formulation on SS is higher than that of conventional asphalt, indicating enhanced resistance to moisture displacement. Furthermore, the cross-linked EA network is found to restrict molecular diffusion at the interface, establishing a negative correlation between adhesion strength and diffusion coefficients. Relative concentration profiles reveal that lighter fractions tend to accumulate at the interface, while the cross-linked network introduces steric hindrance that limits asphaltene migration. These molecular-level insights are consistent with macroscopic surface energy measurements and pull-off tests, confirming the improved moisture stability and interfacial durability of EA–SS composites. This study offers a molecular-level perspective on polymer–mineral adhesion and outlines a viable pathway for utilizing steel slag in sustainable pavements.

Keywords: Epoxy asphalt; Steel slag; Interfacial adhesion; Molecular dynamics simulation; Surface free energy; Moisture susceptibility

1. Introduction

With the continuous development of transportation infrastructure in China, the mileage of highways continues to climb, and the demand for high-quality road aggregates has shown rapid growth. However, the excessive exploitation of high-quality natural basalt and limestone has not only led to the increasing depletion of non-renewable mineral resources but also caused severe mountain destruction and ecological imbalances [1, 2]. In this context, actively exploring the resource utilization of industrial solid waste has become an important direction for promoting green transportation construction and achieving the "Dual Carbon" goals. As the primary by-product of the steel smelting process, steel slag (SS) suffers from a low comprehensive utilization rate due to technical bottlenecks. Long-term open-air stockpiling not only occupies vast land resources but also constitutes a potential source of pollution for soil and groundwater [3-5]. In terms of material characteristics, SS possesses high density, high wear resistance, good angularity, and excellent anti-skid performance, making it a theoretically ideal material to replace natural aggregates in asphalt pavements [6-8]. However, the large-scale application of SS in pavement engineering still faces severe challenges. Unlike natural aggregates with relatively stable mineral components, the mineral composition of SS is extremely complex, containing large amounts of active components such as free oxides. During service, moisture intrusion can easily trigger the expansion of SS, causing early distress such as interfacial stripping and raveling, which severely restricts the pavement durability of SS asphalt mixtures [9, 10].

To address pavement distress under heavy loads and complex environments, epoxy asphalt (EA) has received significant attention due to its superior mechanical properties. As a thermosetting material, EA forms an irreversible three-dimensional cross-linked network during the curing process, endowing the material with extremely high strength, high-temperature resistance, and fatigue

resistance [11, 12]. Based on these superior properties, EA has been widely applied in paving projects for long-span steel bridge decks where requirements for material performance are extremely high [13, 14]. Although EA has achieved great success in the field of special paving, the potential for application in SS asphalt pavements has not yet been fully explored, limited by high material costs and strict construction windows. Theoretically, utilizing the high polarity and cross-linking curing characteristics of epoxy resin can effectively mitigate the poor moisture stability of SS [15]. However, the mechanism of the strong polarity binder–high activity aggregate combination at the microscopic level still requires further investigation.

It is well established that the interfacial adhesion performance between asphalt and aggregates acts as a core factor determining the durability of the mixture, directly influencing the resistance to stripping of the pavement under the coupling effects of moisture and mechanical loads [16, 17]. Existing research mostly focuses on evaluating adhesion strength through macroscopic methods such as pull-off tests, boiling tests, or freeze-thaw splitting tests [18, 19]. Although these methods can characterize the final failure state and macroscopic performance of materials, they are limited by the scale of observation. Consequently, it is difficult to directly observe the microscopic physicochemical changes in the interfacial region, resulting in a lack of theoretical explanation for the interfacial mechanism from the micro-nano perspective. On one hand, the microscopic interaction mechanism between the special polar components introduced by the epoxy modification system and the complex mineral phases on the surface of SS has not yet been clarified. On the other hand, there is also a lack of in-depth analysis regarding the influence of the thermosetting cross-linked network structure on the wetting behavior and molecular diffusion dynamics of the binder on the surface of aggregates.

In recent years, molecular dynamics (MD) simulation technology has been widely introduced into the research of asphalt materials, becoming an effective tool for analyzing microscopic interfacial

behavior [20, 21]. MD simulations can break through the limitations of the observation scale in macroscopic experiments and quantitatively characterize the interaction energy and movement trajectories between molecules at the atomic level. This provides a scientific means to deeply reveal the adsorption mechanism of polar components and the steric hindrance effect of the cross-linked network mentioned above. This not only helps to elucidate the bonding nature of the interface between asphalt and aggregates but also enables dynamic analysis of the interfacial evolution process under different environments [22, 23]. However, previous studies still have room for improvement regarding the authenticity and complexity of the simulation systems, making it difficult to fully cover the diverse mineral components of SS and the special cross-linked structure of EA. Therefore, constructing high-precision molecular models capable of truly reflecting material characteristics is key to accurately clarifying the interfacial adhesion mechanism and filling the gaps in existing research.

To address the challenges mentioned above, this study employs MD simulations combined with laboratory experiments. Through a comparative analysis with basalt and limestone aggregates, the research systematically reveals the interfacial adhesion mechanism between EA and SS, as well as the mechanism of performance improvement. This aims to provide theoretical support for the large-scale application of SS in asphalt pavement engineering. First, a molecular model of EA is constructed, and the reliability of the model is validated. Second, based on the mineralogical composition characteristics of SS, basalt, and limestone, representative crystal surface models are established. On this basis, from a thermodynamic perspective, the work of adhesion, work of debonding, and energy ratio are calculated to quantitatively evaluate the resistance to moisture damage. From a dynamic perspective, the constraint mechanism of the cross-linked network on asphalt molecular diffusion and interfacial evolution behavior is revealed through the analysis of mean square displacement and

relative concentration distribution. Finally, the validation is conducted by combining results from laboratory experiments, such as surface energy tests and pull-off tests. The results of the research elucidate the improvement mechanism of EA regarding the moisture stability and durability of SS asphalt mixtures at the molecular level. Furthermore, this study provides scientific support for the engineering application of SS in high-performance and sustainable asphalt pavements.

2. Materials and methods

2.1. Raw Materials

The raw materials used in this study primarily included 60-80 pen grade base asphalt (BA), an epoxy resin system (EPS), SS, basalt, and limestone. Specifically, the BA was provided by Nanjing Jinling Asphalt Industry Co., Ltd. (Nanjing, China); the EPS consisted of an epoxy resin, an amine curing agent, and a toughening agent; the SS was sourced from Jiangsu Yonggang Group Co., Ltd. (Suzhou, China); and the basalt and limestone were supplied by Suzhou Sanchuang Pavement Engineering Co., Ltd. (Suzhou, China). The basic properties of these raw materials were tested in accordance with the "Standard test methods of bitumen and bituminous mixtures for highway engineering" (JTG E20-2011), "Test Methods of Aggregate for Highway Engineering" (JTG E42-2005), and "Steel Slag for Road" (GB/T 25824-2010) [24-26]. All materials met the requirements of the aforementioned specifications, and the test results are presented in Table 1.

Table 1. Basic properties of raw materials

Material type	Basic property
BA	Penetration (25°C,100 g, 5 s): 68.6 (0.1mm); Ductility (5 cm/min, 10°C): 26.5 cm; Softening point: 47.4 °C; Density (25°C): 1.035 g/cm^3.
Epoxy resin	Viscosity (23°C): 16900 mPa·s; Epoxide equivalent: 194 g/eq; Exterior condition: Colorless transparent liquid.
Curing agent	Viscosity (23°C): 2500 mPa·s; Amine value: 209 mgKOH/g; Exterior condition: Light yellow liquid.

Toughening agent	Viscosity (23°C): 10000 mPa·s; Exterior condition: Brown liquid.
SS	Density: 3.476 g/cm^3; Hygroscopic rate: 1.87%; Crush value: 13.0%; Abrasion value: 13.9%.
Basalt	Density: 2.874 g/cm^3; Hygroscopic rate: 0.98%; Crush value: 10.2%; Abrasion value: 14.1%.
Limestone	Density: 2.783 g/cm^3; Hygroscopic rate: 1.12%; Crush value: 10.3%; Abrasion value: 14.2%.

2.2. Model building and validation

2.2.1. Selection of MD simulation parameters

MD simulations were employed to model the asphalt-aggregate system. The Velocity-Verlet algorithm was selected because it maintains low computational complexity while ensuring computational accuracy, effectively solving the motion state of particles through iteration [27]. Considering the chemical heterogeneity of the epoxy asphalt and the presence of ionic and polar sites on the aggregate surface, the COMPASS III force field was adopted in this study to characterize the epoxy asphalt–aggregate interface system [28]. The COMPASS force field family is a Class II, condensed-phase-optimized force field, whose parameters are fitted using both ab initio calculations and experimental data. Its energy expression includes not only diagonal valence terms but also cross-coupling terms between internal coordinates, enabling a precise description of the molecular conformations and condensed-phase behaviors of complex organic materials [29, 30]. Compared with the CVFF force field, which was developed primarily for organic and biomolecular systems, COMPASS III possesses a broader parameter set coverage for condensed-phase organic materials and selected inorganic materials. Although the PCFF force field also adopts a Class II functional form, COMPASS III is equipped with an updated parameter system that allows both the asphalt phase and the aggregate phase to be described within a unified force field framework, avoiding the uncertainties associated with mixing multiple independently parameterized force fields. Previous studies have confirmed that the COMPASS force field family can be effectively used to predict asphalt density, cohesive properties, molecular aggregation behaviors, and asphalt–mineral interfacial adhesion

properties [20, 31, 32].

The presence of charged or partially charged sites on the mineral surface generates Coulombic interactions that cannot be adequately characterized by a simple cutoff method; therefore, the Ewald summation method was employed in this paper to calculate the long-range electrostatic interactions. Ewald summation can account for electrostatic interactions with periodic images in both real and reciprocal spaces simultaneously, reducing truncation errors in periodic ionic systems [33]. Van der Waals interactions were evaluated using the atom-based calculation method, with a cutoff distance set to 18.5 Å. Compared to Coulombic interactions, dispersion interactions decay more rapidly with distance; directly performing pairwise summation within a sufficiently large cutoff radius can efficiently handle the interface model constructed in this study. This cutoff distance was selected based on previous related molecular dynamics studies on asphalt–minerals, where similar parameter settings can obtain stable non-bonded interaction energies and interfacial properties [20, 34].

2.2.2. Molecular model of BA

Given the extreme complexity of the chemical composition of asphalt, MD simulations typically employ an assembly method, which involves constructing amorphous cells by arranging representative molecules according to the ratio of SARA (Saturates, Aromatics, Resins, and Asphaltenes). Although early studies often adopted simplified three-component or four-component models, this study selected the 12-component all-atom model representing SHRP AAA-1 asphalt proposed by Li and Greenfield to more authentically reproduce the microstructure and thermodynamic properties of asphalt [35]. This model has been widely validated to possess higher consistency with experimental data compared to traditional simplified models in the prediction of density, coefficient of thermal expansion, and rheological properties. Furthermore, considering the strict requirements for the stoichiometric ratio during the subsequent construction of the EA cross-

linked network, directly adopting the simplified number of molecules from the literature could lead to errors in mass fraction. Therefore, this study performed a proportional scaling up of the molecular population of the original model, constructing a large-scale system containing a greater number of particles. Theoretically, proportionally enlarging the system size under periodic boundary conditions does not change intensive thermodynamic properties such as system density and cohesive energy density; instead, it can effectively mitigate finite-size effects [36]. Furthermore, the scaling factor is selected based on the requirement of "mass resolution". Due to the discrete nature of the molecular weights of the cross-linked units, scaling up the base asphalt matrix can significantly reduce stoichiometric rounding errors, making the mass fractions of the epoxy formulations closer to the experimental design values [35]. The detailed molecular formulas and quantities of each component are presented in Table 2, and the established initial equilibrium configuration is illustrated in Fig. 1.

Table 2. Molecular composition and mass fractions of the four components in the BA model

Representative component and molecular constituent		Molecular formula	Number of molecules	Mass fraction /%
Saturates	Squalane	$C_{30}H_{62}$	8	5.2
	Hopane	$C_{35}H_{62}$	8	5.9
Aromatics	PHPN	$C_{35}H_{44}$	22	15.7
	DOCHN	$C_{30}H_{46}$	26	16.2
Resins	Quinolinohopane	$C_{40}H_{59}N$	8	6.8
	Thioisorenieratane	$C_{40}H_{60}S$	8	5.9
	Trimethylbenzeneoxane	$C_{29}H_{50}O$	30	6.4
	Pvridinohopane	$C_{36}H_{57}N$	8	6.2
	Benzobisbenzothiophene	$C_{18}H_{10}S_2$	10	13.4
Asphaltenes	Asphaltene-phenol	$C_{42}H_{54}O$	6	5.3
	Asphaltene-pyrrole	$C_{66}H_{81}N$	4	5.5
	Asphaltene-thiophene	$C_{51}H_{62}S$	6	6.5

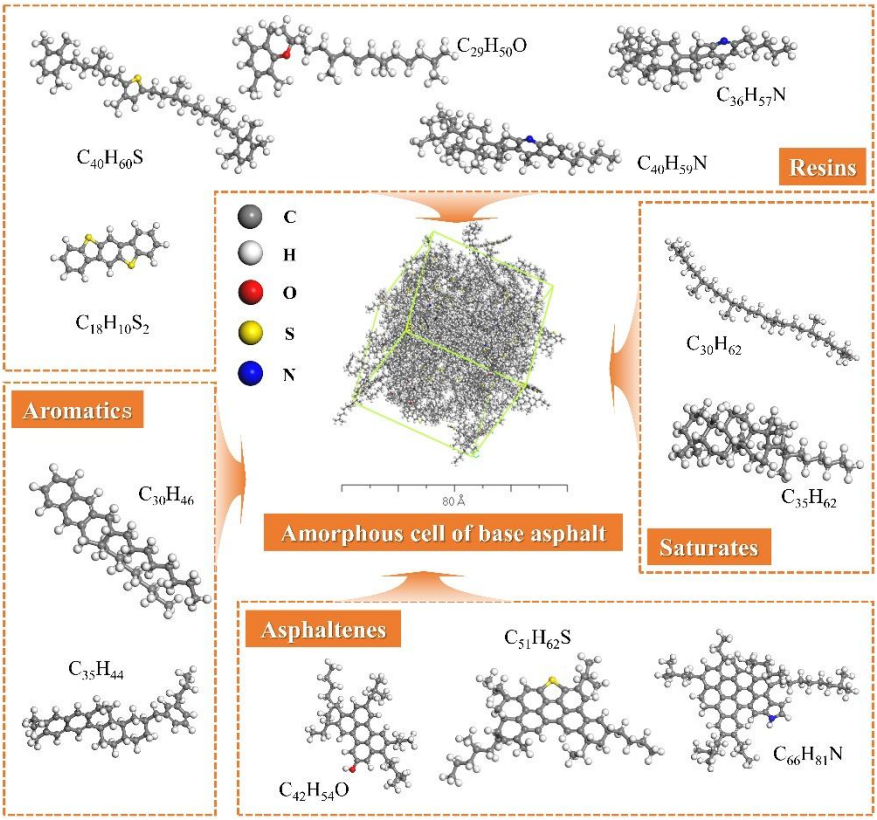


Fig. 1. Construction of the BA molecular model

2.2.3. Molecular models of EPS and EA

To construct an accurate EPS model, the solubility parameters (δ) at varying degrees of polymerization were first calculated based on the cohesive energy density (*CED*) theory to determine the optimal molecular chain length for each component. The calculation results indicated that the δ of the system tends to converge and stabilize when the degree of polymerization for the epoxy resin monomer is n=0 and for the toughening agent is n=10. Consequently, this configuration was selected as the foundational model [20]. On this basis, to investigate the influence of EPS content on interfacial performance, two hybrid systems were constructed. The optimized EPS components (epoxy resin, curing agent, and toughening agent) were mixed with the aforementioned BA model according to mass ratios. Models with EPS mass fractions of 20% (EP20) and 40% (EP40) were established and designated as EA20 and EA40, respectively. According to previous studies, EA20 and EA40 are typically suitable for ordinary pavements and bridge deck pavements, respectively; thus, they were

selected as the research objects in this study [11, 15]. The molecular mixing ratios are presented in Table 3. All initial models were constructed within amorphous cells with an initial low density set to 0.1 g/cm^3 to prevent initial atomic overlap and facilitate uniform mixing.

Table 3. EPS composition and its molecular proportion in the EA model

Material system	Component	Molecular formula	Number of molecules	Mass fraction/%
EP20	Epoxy resin	$C_{21}H_{24}O_4$	27	20.91
	Curing agent	$C_{18}H_{37}N$	23	
	Toughening agent	$C_{40}H_{56}N_2O_4$	3	
EP40	Epoxy resin	$C_{21}H_{24}O_4$	70	40.31
	Curing agent	$C_{18}H_{37}N$	59	
	Toughening agent	$C_{40}H_{56}N_2O_4$	7	

The curing process of EPS was implemented via a Perl script program, which simulates the stepwise cross-linking reaction between epoxy groups and amine curing agents based on distance criteria [37, 38]. The reaction mechanism was defined as a diffusion-controlled process; that is, a chemical bond is generated when reactive atoms (the C atom of the epoxy group and the N atom of the curing agent) enter a specific cutoff distance. The specific procedure is as follows: First, the initial search radius was set to 4.5 Å. If reactive sites existed within this range, a C-N bond was formed. Subsequently, energy minimization was performed on the new topology immediately to eliminate local high-energy stress caused by bond formation. If the energy fluctuation remained within the threshold, the bond was retained. Following this, the cutoff radius was expanded stepwise to 15 Å with an increment of 0.5 Å, and the search-bond-relax process was executed cyclically until the preset degree of curing was reached or no further reaction sites were available. Ultimately, an EA system featuring a three-dimensional network structure was generated.

All simulations were conducted using the Forcite module based on the COMPASS III force field.

To eliminate anisotropy and simulate macroscopic bulk materials, PBC were applied in all three directions. The simulation protocol comprised the following key stages: i) Geometry Optimization: Energy minimization was performed on both the initial and cross-linked structures using the Smart algorithm with 20,000 iteration steps. ii) Dynamic Relaxation: Simulations under the NVT ensemble for 500 ps at 298.15 K and the NPT ensemble for 500 ps at 1 atm were conducted sequentially to achieve the initial equilibrium of density and energy for the system. iii) Annealing Treatment: To eliminate local metastable structures potentially resulting from rapid cross-linking, five cycles of simulated annealing were executed. The temperature oscillated cyclically between 200 K and 600 K, with each cycle containing 10 temperature gradients. iv) Production Sampling: The fully annealed system underwent a final production run of 500 ps under the NPT ensemble at 298.15 K and 1 atm. During the simulation, temperature and pressure were controlled by the Nosé-Hoover-Langevin thermostat and the Berendsen barostat, respectively. Van der Waals interactions were calculated using the Atom-based summation method with a cutoff radius of 12.5 Å, while electrostatic interactions were treated using the Ewald summation method with an accuracy of 10^{-4} kcal/mol and a cutoff radius of 12 Å. The constructed molecular model of EA is illustrated in Fig. 2.

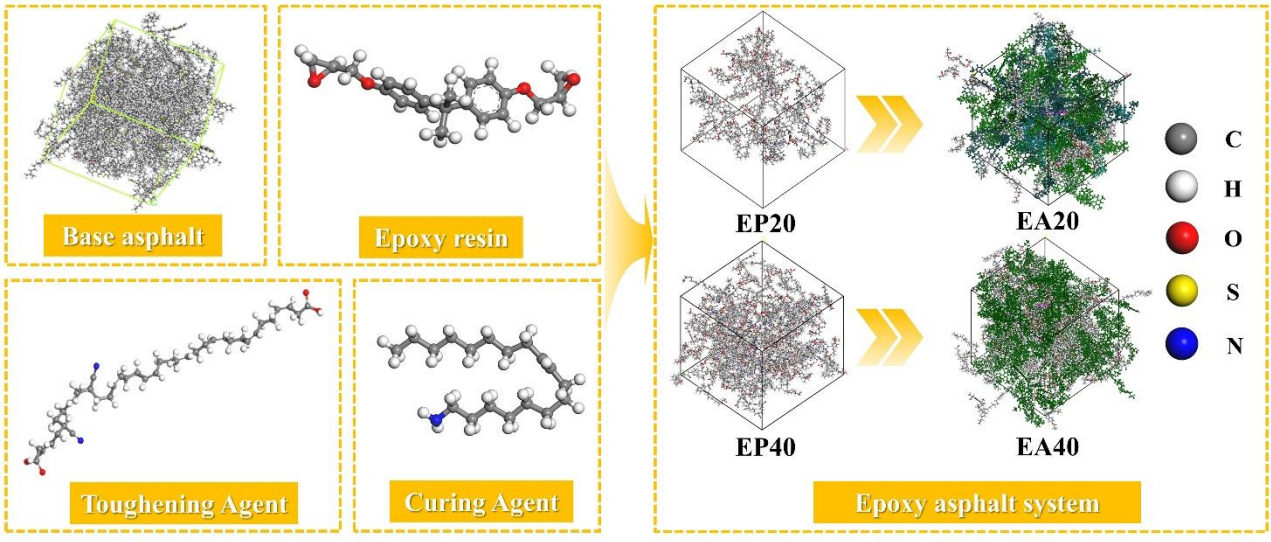


Fig. 2. Construction of EA molecular models

2.2.4. Validation of EA molecular models

To comprehensively evaluate the accuracy of the molecular models and the applicability of the force field parameters, dynamic equilibrium simulations of 500 ps were first conducted on the BA, EA20, and EA40 systems under the NPT ensemble at standard conditions of 298.15 K and 1 atm. As presented in Table 4, the equilibrium density of each system aligns well with experimental measurements and data reported in the literature, with deviations controlled within a reasonable range. The minor discrepancies between simulated and actual values are primarily due to physical simplifications. On one hand, although the 12-component asphalt model covers the characteristics of the four SARA components, it cannot fully reproduce the extreme molecular complexity of actual heavy asphaltenes. On the other hand, the epoxy resin monomer in the model was set to a fixed degree of polymerization (n=0), neglecting the influence of polydisperse oligomers on the free volume of the system in the actual material [20]. Nevertheless, the verification confirms that the model accurately reflects the bulk packing density and macroscopic structural characteristics of the material, providing a reliable structural foundation for subsequent simulations. Based on *CED* theory, the δ of each component was further calculated to quantitatively evaluate the compatibility between EPS and the asphalt matrix at the microscopic level. The results indicate that the differences in δ among the components in EA are strictly maintained within the empirical compatibility threshold. This outcome not only validates the accuracy of the COMPASS III force field in describing the non-bonded interaction potential between molecules in complex organic-inorganic hybrid systems but also confirms, from the perspective of thermodynamic equilibrium, that a stable miscible structure has formed between the epoxy cross-linked network and the asphalt matrix. The absence of micro-phase separation indicates that the model possesses good thermodynamic stability.

Table 4. Comparison of MD simulation parameters for different asphalt models with references

Item	BA model	EA20 model	EA40 model
Simulated density/(g/cm^3)	0.997	0.994	0.991
Reference density/(g/cm^3)	1.035	0.997–1.040 [39, 40]	
Simulated Solubility Parameter/ (J/m^3) $^{1/2}$	17.9	16.28	16.09
Reference Solubility Parameter/ (J/m^3) $^{1/2}$	15.3–23.0	15.146–18.221 [39, 40]	

Given the decisive role of polar groups in the curing kinetics and dielectric properties of EA, geometry optimization and analysis of electronic properties were performed on the cross-linking intermediates within the EA system using the DMol3 module. The BLYP density functional under the generalized gradient approximation was employed, coupled with Semi-core pseudopotentials for the treatment of core electrons. As shown in Fig. 3, Mapping analysis of ESP revealed significant heterogeneity in charge distribution: the carbon backbone region primarily exhibited electrical neutrality (green regions), whereas areas of high electron density (red/negative potential) were highly concentrated around oxygen-containing functional groups. Quantitative polarity ranking indicated that the -OH generated by the ring-opening reaction exhibited the highest polarity strength, followed by unreacted epoxy groups, while ether bonds and C-N bonds at the cross-linking points possessed relatively weaker polarity. This characteristic of the electronic structure aligns perfectly with conclusions regarding the dielectric relaxation mechanism of epoxy resins found in literature [41], validating the chemical rationality of the cross-linking reaction path and the structure of the product from a quantum mechanical perspective.

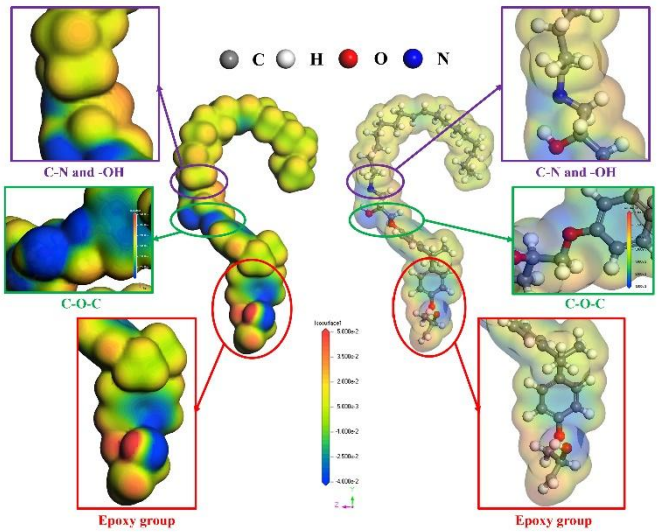


Fig. 3. Electrostatic Potential Distribution of the EPS Curing Intermediate

2.2.5. Molecular models of aggregates

(1) Model selection for aggregates

Given the diverse sources and varying cooling conditions of SS, the mineral composition exhibits significant heterogeneity and complexity. Research by Qian et al. [42] indicates that, despite substantial differences in minor components among SS from different origins, the primary mineral phases typically consist of silicates, ferrites, and oxides. To construct a SS model with general applicability for MD simulations, this study performed a simplified screening based on the principle of dominant mineral phases, while ignoring trace crystallographic variants. Ultimately, five key minerals were selected as representative model components for SS: C_2S, $Ca(OH)_2$, C_2F, Fe_3O_4, and the RO phase (represented by CaO). These components cover the main cementitious active phases and metal oxide phases in SS, effectively characterizing the physicochemical properties of the surface.

In comparison to SS, basalt and limestone, as natural mined ores, possess relatively stable mineralogical compositions. Based on XRD test results and literature [43-45], the primary rock-forming minerals of basalt are plagioclase and olivine, while limestone is dominated by carbonate minerals. Therefore, this study selected albite ($Na[AlSi_3O_8]$) and anorthite ($Ca[Al_2Si_2O_8]$) from the plagioclase as representative molecular models for basalt; calcite ($CaCO_3$) was selected as the single

dominant mineral model for limestone. This simplified treatment retains the typical surface energy characteristics of the aggregates while ensuring computational efficiency.

The initial crystal structure parameters for all selected minerals were exported from the Inorganic Crystal Structure Database (ICSD). In the construction of the simulation, supercells were first established based on the standard unit cells from the ICSD. Subsequently, cutting was performed along specific cleavage planes to expose the most representative crystal surfaces. Finally, aggregate slab models were constructed for the analysis of interfacial interaction. The chemical formulas and lattice parameters for each representative mineral are detailed in Table 5 and Table 6.

Table 5. Representative mineral chemical formulas and structures in SS

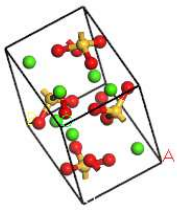
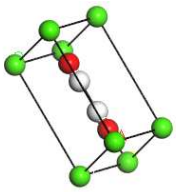
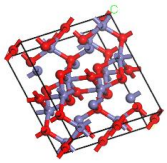
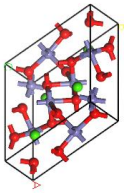
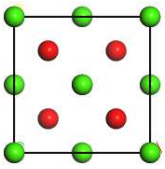
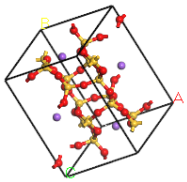
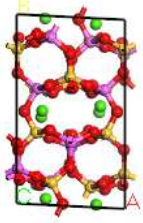
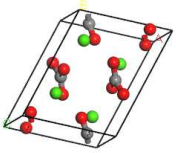
Mineral Chemical Formula	Representative Molecular Structure	Lattice Parameter						
		Space Group	Lattice Vector Lengths/Å			Interaxial Angles/°		
			a	b	c	α	β	γ
C_2S		P121/N1	5.51	6.67	9.32	90	94.45	90
$Ca(OH)_2$		P-3M1	3.58	3.58	4.90	90	90	120
Fe_3O_4		BBMM	9.27	9.23	2.74	90	90	90
C_2F		PNMA	10.66	9.20	3.01	90	90	90
CaO		FM-3M	5.27	5.27	5.27	90	90	90

Table 6. Representative mineral chemical formulas and structures in basalt and limestone

Mineral Chemical Formula	Representative Molecular Structure	Lattice Parameter						
		Space Group	Lattice Vector Lengths/Å			Interaxial Angles/°		
			a	b	c	α	β	γ
$Na[AlSi_3O_8]$		C-1	8.153	12.86	7.107	93.52	116.4	90.25
$Ca[Al_2Si_2O_8]$		P-1	8.196	12.90	14.20	93.13	115.9	91.25
$CaCO_3$		P121/C1	6.334	4.948	8.033	90	107.9	90

(2) Establishment of aggregate molecular models

To construct a realistic asphalt-aggregate interface, it is necessary to determine the cleavage plane with the highest thermodynamic stability for each mineral. The Morphology Method was employed to predict the growth habit of the crystals. This method relies on the Bravais-Friedel-Donnay-Harker theory, which postulates that the growth rate of a crystal face is directly proportional to the attachment energy [46, 47]. By calculating the section energy of various low-index crystal planes, the most active surface possessing the maximum attachment energy was selected as the direction for cutting. The preferred cleavage planes and relevant parameters for each representative mineral are detailed in Table 7.

Table 7. Selection of reactive crystal surfaces for aggregate minerals

Aggregate Type	Mineral Chemical Formula	Selected Surface（k h l）
SS	C_2S	(0 1 1)
	$Ca(OH)_2$	(1 -1 0)
	Fe_3O_4	(1 1 1)

	C_2F	(1 1 0)
	CaO	(1 0 0)
Basalt	$Na[AlSi_3O_8]$	(1 -1 0)
	$Ca[Al_2Si_2O_8]$	(0 1 0)
Limestone	$CaCO_3$	(1 0 0)

Using C_2S as an example, the unit cell was cleaved along the direction of the selected cleavage plane. Since the dimensions of the original unit cell are small (merely 5.5×11.5 Å), they are insufficient to eliminate finite-size effects within the interfacial simulation. Consequently, a supercell with dimensions of approximately 55.05×55.05 Å was constructed by expanding the lattice within the XY plane. Subsequently, the two-dimensional surface model was transformed into a three-dimensional periodic slab model, incorporating a vacuum layer of sufficient thickness to isolate periodic image interactions along the Z-direction. The topology of all aggregate models underwent force field verification, and unnecessary explicit chemical bonds were removed. This step ensures that ionic interactions are accurately described by non-bonded potential energy terms. Fig. 4 illustrates the construction process of the aggregate slab models.

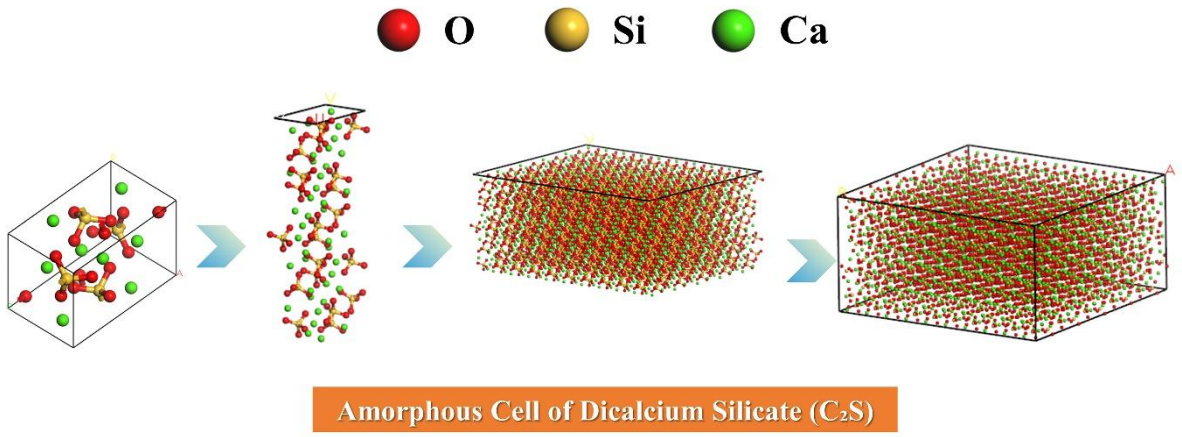


Fig. 4. Schematic diagram of the processing workflow for constructing mineral unit cell models

Given that the initial mineral structures selected in this study were derived directly from the ICSD, the lattice parameters have undergone rigorous experimental validation. Existing literature indicates that in simulations of the asphalt-aggregate interface, performing additional geometric

optimization on rigid mineral substrates makes a minimal contribution to the reduction of the total energy of the system and has a negligible impact on the interfacial adsorption configuration [48]. Consequently, to preserve the experimental authenticity of the crystal structures and enhance computational efficiency, no further geometric relaxation was performed on the mineral aggregate models following construction.

2.2.6. EA-aggregate interface molecular models

To construct a bilayer interface model under PBC, it is necessary to address the issue of lattice mismatch between the amorphous asphalt cell and the aggregate mineral cell in the XY plane. Taking the XY dimensions of the aggregate supercell as the reference, the lattice parameters of the asphalt model were adjusted for compatibility. Since forced lattice deformation can induce bond stretching and molecular conformational distortion, leading to a significant increase in the potential energy of the system, strict geometry optimization was performed on the adjusted asphalt model prior to assembly, as shown in Fig. 5. This step effectively eliminated high-energy structures and ensured that the asphalt bulk phase reached a state of thermodynamic relaxation under the new lattice dimensions.

The optimized asphalt model was superimposed upon the mineral slab model to construct an asphalt-aggregate bilayer interface system. To eliminate non-physical van der Waals interactions arising from periodic images in the direction of the Z-axis, a vacuum slab with a thickness of 140 Å was established above the asphalt layer. In the subsequent simulation, all atoms within the mineral aggregate layer were set to "Fixed" to simulate the mechanical support provided by macroscopic bulk materials. Upon completion of the assembly, energy minimization was applied to the entire interfacial model using the Smart algorithm. This step aimed to eliminate local high-energy spots resulting from atomic overlap or steric hindrance at the stacking interface, ultimately obtaining an equilibrated dry interface model.

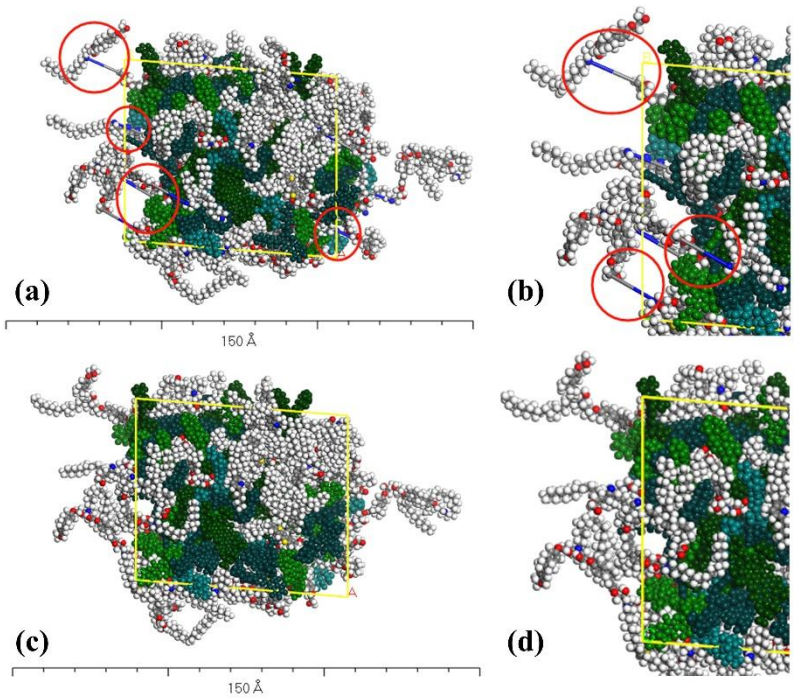


Fig. 5. Optimization of the asphalt model:

(a) EA40 after lattice parameter adjustment; (b) Local detail of EA40 in (a); (c) EA40 after geometry optimization with adjusted lattice parameters; (d) Local detail of EA40 in (c).

To investigate the mechanism of interfacial stripping under moisture conditions, a hydrated interface model was further constructed. Referring to relevant literature, this study first established a pre-equilibrated amorphous water layer containing 200 water molecules, and placed this water layer between the mineral surface and the asphalt layer to form an aggregate-water-asphalt sandwich structure [33, 49]. The equivalent water film thickness corresponding to this number of water molecules is approximately 2.0 Å, which is smaller than the kinetic diameter of a single water molecule of about 2.8 Å. Therefore, this model system represents a not fully saturated state, which is used to simulate competitive adsorption behavior following the intrusion of moisture into the interfacial zone. Taking the EA40 system as a representative example, the construction process and final configurations of the interface under dry and wet states are illustrated in Fig. 6 and Fig. 7, respectively.

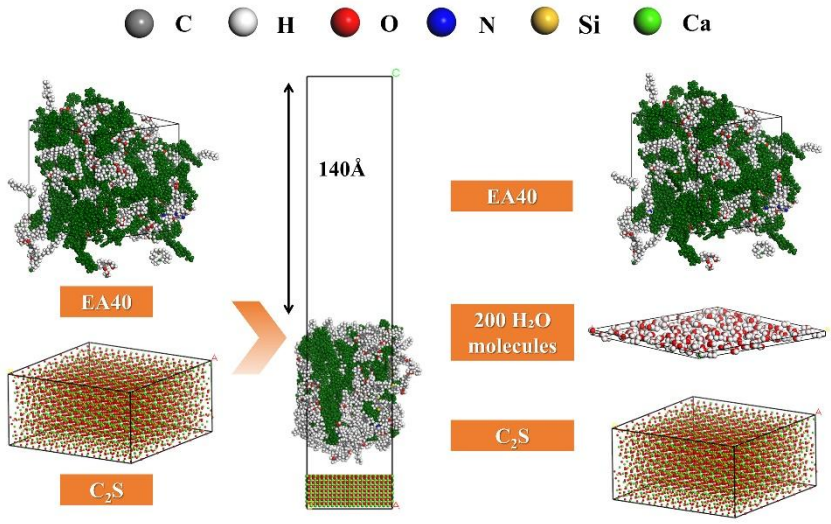


Fig. 6. Workflow for constructing the interfacial molecular model

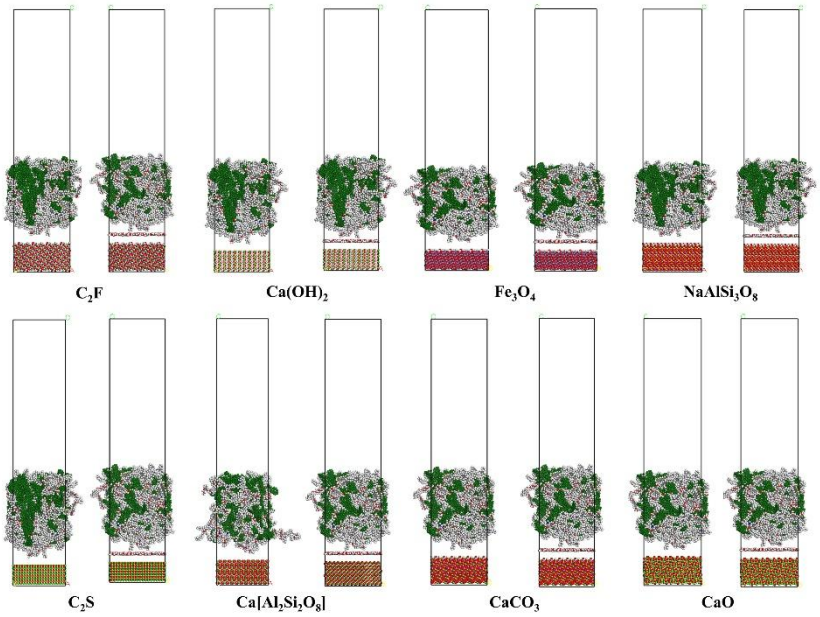


Fig. 7. Constructed interfacial models for EA40 with different mineral substrates

2.3. Methods

2.3.1. Simulation parameters

Prior to the MD simulation, the Smart algorithm was employed to perform geometry optimization on the assembled interface model (5000 iterations). This step aimed to eliminate local stress and excess potential energy generated during the initial configuration process, ensuring that the system reached a reasonable state of minimum energy. To investigate the influence of service temperature on interfacial adhesion behavior, 298 K (25°C) and 333 K (60°C) were selected to

represent the ambient and high-temperature operating conditions of road pavements, respectively. MD simulations with a duration of 500 ps were conducted for all interface systems under the NVT ensemble. This duration suffices to allow the system to attain thermodynamic equilibrium and provides adequate statistical data for the subsequent analysis of trajectories.

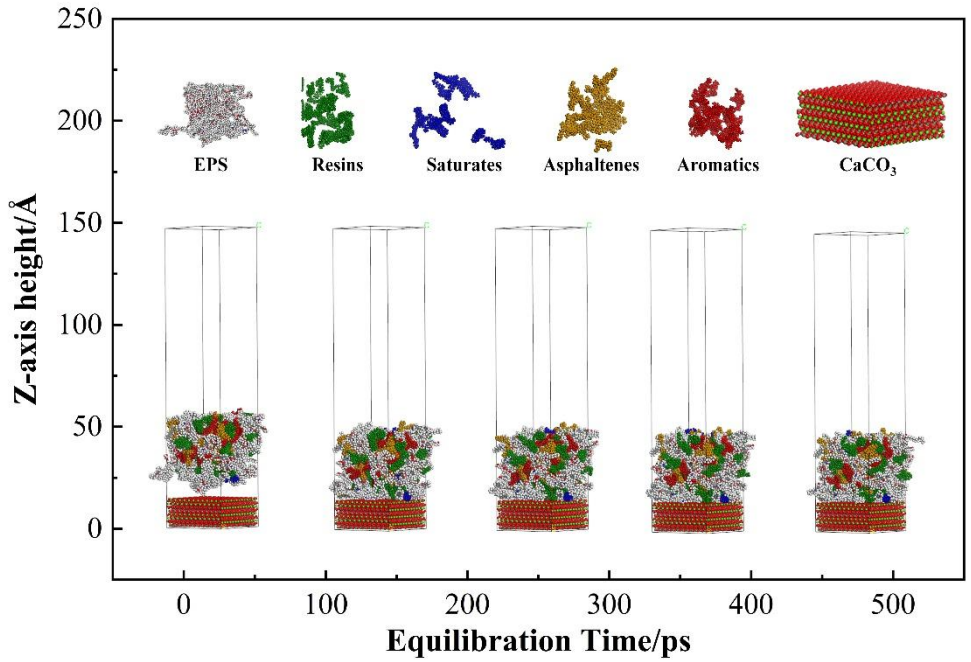


Fig. 8. Evolution of the EA-Mineral Interface Model during 500 ps of Equilibration.

During the simulation process, van der Waals interactions were calculated using the Atom-based method with a cutoff radius set to 15.5 Å to ensure the computational accuracy of long-range interactions. Electrostatic interactions were treated using the PPPM (Particle-Particle Particle-Mesh) algorithm. Upon completion of the simulation, the trajectory files for BA, EA, and various aggregates in the equilibrium state were exported for the subsequent analysis of interfacial energy and structural characteristics, as illustrated in Fig. 8.

2.3.2. Adhesion properties

To quantify the adhesion performance between EA and different mineral aggregates (SS, basalt, and limestone), the interfacial interaction energy (E_{int}) was calculated based on MD trajectories. On this basis, the work of adhesion ($W_{adhesion}$) was introduced as a key evaluation index, defined as the

energy required to separate a unit area of the interface into two independent free surfaces [50]. E_{int} and $W_{adhesion}$ are calculated using Eqs. (1) and (2). Thermodynamically, a negative interaction energy indicates the existence of attractive forces at the interface. A larger $W_{adhesion}$ indicates that the energy required to overcome interfacial bonding is higher, meaning that the adhesion performance between asphalt and aggregates under dry conditions is superior.

Considering that moisture intrusion is a core factor leading to early distress in asphalt mixtures, this study simulated the interfacial bonding performance of the asphalt-aggregate interface eroded by moisture. It is assumed that moisture penetration destroys the original close contact, leading to competitive adsorption. To this end, the work of debonding $W_{debonding}$ was introduced to evaluate the damaging effect of moisture on interfacial bonding ability. According to Eqs. (3)-(5), $W_{debonding}$ is defined as the difference in free energy of the system as it transforms from a dry bonded state to a wet separated state. Specifically, this calculation quantifies the process where the original asphalt-aggregate interface vanishes due to moisture intrusion and is replaced by new asphalt-water and aggregate-water interfaces.

To comprehensively evaluate the resistance of the interface system to moisture damage, the energy ratio (*ER*) was further introduced as a dimensionless evaluation index by combining thermodynamic data on dry adhesion and wet stripping, as shown in Eq. (6). The *ER* reflects the tendency of the interface to maintain bonding in a humid environment; a higher *ER* implies that the asphalt-aggregate interface is thermodynamically more stable and possesses stronger resistance to water displacement and durability.

$$\Delta E_{\text{inter-as-ag}}=E_{\text{total}}-\left(E_{\text{asphalt}}+E_{\text{aggregate}}\right) \tag{1}$$

$$W_{\text{adhesion}}=\frac{\Delta E_{\text{int-as-ag}}}{A} \tag{2}$$

$$\Delta E_{\text{inter-ag-w}}=E_{\text{total-ag-w}}-\left(E_{\text{aggregate}}+E_{\text{water}}\right) \tag{3}$$

$$\Delta E_{\text{inter-as-w}}=E_{\text{total-as-w}}-\left(E_{\text{asphalt}}+E_{\text{water}}\right) \quad (4)$$

$$W_{\text{debonding water}}=\frac{\left(\Delta E_{\text{inter-as-w}}+\Delta E_{\text{inter-ag-w}}\right)-\Delta E_{\text{inter-as-ag}}}{A} \quad (5)$$

$$ER=\frac{|W_{\text{adhesion}}|}{W_{\text{debonding water}}} \quad (6)$$

Where, $\Delta E_{\text{inter-as-ag}}$ represents the interaction energy within the interfacial system of asphalt and aggregate (kcal/mol); E_{total} denotes the total energy of the combined system of aggregate and asphalt (kcal/mol); E_{asphalt} signifies the energy of the binder component within the system (kcal/mol); $E_{\text{aggregate}}$ stands for the energy of the aggregate (kcal/mol); A refers to the cross-sectional area of the interfacial contact region (Å²); W_{adhesion} represents the work of adhesion for the asphalt-aggregate system under dry conditions (mJ/m^2); $\Delta E_{\text{inter-ag-w}}$ indicates the interaction energy between the asphalt layer and the water molecule layer (kcal/mol); $\Delta E_{\text{inter-as-w}}$ denotes the interaction energy between the water molecule layer and the aggregate layer (kcal/mol); $\Delta E_{\text{inter-as-ag}}$ refers to the interaction energy between asphalt and aggregate (kcal/mol).

2.3.3. Diffusion behavior of EA

To elucidate the microscopic dynamic behavior of the EA system, Mean Square Displacement (*MSD*) was employed to characterize the mobility of polymer chain segments and molecular migration rates, as expressed in Eq. (7). The magnitude of *MSD* directly reflects the interplay between the fluidity and rigidity of the material [51]. A higher *MSD* value implies that molecular chains possess greater degrees of freedom in movement, which facilitates the self-healing of micro-cracks and stress relaxation. Conversely, a lower *MSD* value indicates that molecules are subject to significant restriction (the confinement effect), corresponding to enhanced rigidity of the system and resistance to deformation at high temperatures. Therefore, analysis of *MSD* allows for an effective evaluation of the equilibrium mechanism between toughness and high-temperature stability within

the material.

In a fully relaxed system, *MSD* typically exhibits a linear growth trend over time. Based on the Einstein relation, the self-diffusion coefficient (*D*) of the molecules can be quantified via the slope of the linear region of the *MSD* curve. When the simulation time is sufficiently long, *D* is defined as one-sixth of the slope of the *MSD*, as shown in Eq. (8). This parameter provides a quantitative description of interfacial dynamics, intuitively reflecting the extent to which adsorption by different mineral surfaces restricts or promotes the diffusion behavior of EA molecules.

$$\mathrm{MSD}(t)=\left\langle \Delta r_i(t)^2 \right\rangle=\left\langle (r_i(t)-r_i(0))^2 \right\rangle \tag{7}$$

$$D=\frac{r(t)^2}{6t} \tag{8}$$

Where, $\Delta r_i(t)^2$ represents the position vector of atomic group *i* at time *t*; $r_i(t)$ denotes the position vector of atomic group *i* at time *t*; $r_i(0)$ signifies the initial reference position of the atomic group; ⟨ ⟩ denote the ensemble average over all selected atomic groups; $r(t)^2$ refers to the displacement of the molecule.

2.3.4. Compositional distribution characteristics of EA

Although *MSD* effectively characterizes the dynamic migration rate of molecules, it fails to provide structural information regarding the spatial arrangement and packing patterns of molecules at the interface. In the asphalt-aggregate interface system, forces of solid-liquid interaction drive asphalt components to undergo directional migration toward the mineral surface, resulting in the formation of specific adsorption layers. To accurately analyze the spatial distribution characteristics and layered structure of EA components in the direction perpendicular to the aggregate surface (Z-axis), relative concentration (*RC*) was introduced as a key metric for static structural evaluation. *RC* is defined as the distribution of atomic number density along a specific coordinate axis. The specific calculation method involves dividing the simulation system along the Z-direction into multiple thin

slabs of unit thickness. The quantity of atoms or centroids within each slab is then counted and normalized according to Eqs. (9) and (10). By analyzing the distribution curve of *RC* along the Z-axis, it is possible to intuitively identify enrichment regions and depletion regions of asphalt at the interface, thereby quantifying the thickness and compactness of the interfacial adsorption layer.

$$RC_i = C_i / C_{bulk} \tag{9}$$

$$C_i = N_i / V \tag{10}$$

Where, C_i represents the concentration of the slab; C_{bulk} denotes the concentration of the system; V indicates the volume (cm^3); N_i refers to the number of atoms.

2.3.5. Microscale surface energy test

Based on the theory of surface free energy, this study introduces the work of adhesion (W_{as}) and the work of stripping (W_{aws}) to evaluate the thermodynamic stability of the asphalt-aggregate interface under dry and moist environments, respectively [52]. Defined as the reduction in the free energy of the system when two phases come into contact to form a unit interface, W_{as} is expressed in Eq. (11). A higher value indicates a tighter interfacial bond under dry conditions. To simulate the process of moisture damage, W_{aws} is utilized to characterize the change in Gibbs free energy during the displacement of the asphalt film by moisture, as illustrated in Eq. (12). This model quantifies the resistance of the interface to stripping as the energy difference involved in the transition from an asphalt-aggregate system to aggregate-water and asphalt-water systems, thereby predicting moisture stability from a thermodynamic perspective.

$$W_{as} = 2\sqrt{\gamma_S^d \gamma_L^d} + 2\sqrt{\gamma_S^p \gamma_L^p} \tag{11}$$

$$W_{aws} = W_{aw} + W_{sw} - W_{as} \tag{12}$$

Where, γ^d represents the dispersion component of surface free energy (mJ/m^2); γ^p denotes the polar

463 component of surface free energy (mJ/m^2); γ_S signifies the dispersion component of surface free
464 energy for the solid (mJ/m^2); γ_L refers to the dispersion component of surface free energy for the
465 liquid (mJ/m^2); W_{aws} stands for the work of stripping (mJ/m^2); W_{aw} represents the work of adhesion
466 between asphalt and water (mJ/m^2); W_{sw} indicates the work of adhesion between aggregate and water
467 (mJ/m^2); W_{as} denotes the work of adhesion between asphalt and aggregate (mJ/m^2).

468 The sessile drop method was employed to measure the contact angles on various solid surfaces,
469 as illustrated in Fig. 9. Large particles of SS, basalt, and limestone were selected and polished
470 stepwise to 2000 mesh using a metallographic polishing machine. This step ensured that the surface
471 roughness satisfied the requirements for testing. Subsequently, the polished samples underwent
472 ultrasonic cleaning with distilled water and were dried at 70°C for 2 h to eliminate adsorbed water
473 from the surface. BA, EA20, and EA40 were drop-coated onto glass slides. To simulate performance
474 in the field, the specimens were first leveled at 80°C. Subsequently, the EA specimens were placed
475 in an oven at 60°C for a curing period of 4 d to ensure the completion of the cross-linking reaction.
476 Three probe liquids with known surface energy parameters were selected: distilled water, formamide,
477 and glycerol. The testing instrument employed was a video optical contact angle measuring device
478 (LAUDA Scientific, Model OSA), featuring a measurement range of 0° to 180° and precision
479 controlled within ±0.1°. During the experimental process, a micro-injection system was utilized to
480 deposit droplets precisely onto the flat surface of the asphalt or aggregate. A high-resolution camera
481 captured the droplet profile in real time to fit the contact angle, from which the surface free energy
482 components were calculated based on the extended Fowkes model. To eliminate random errors, at
483 least 3 parallel tests were conducted for each liquid on each substrate, with the arithmetic mean
484 adopted as the final result.

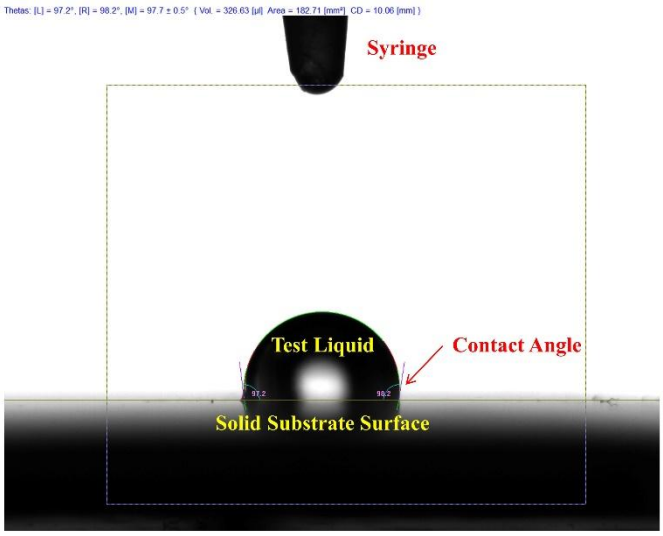


Fig. 9. Contact angle test

2.3.6. Pull-off test

In accordance with the AASHTO T361 standard, the Binder Bond Strength (BBS) test was employed to determine the macroscopic bond strength ($P_{\text{As-Agg}}$) between asphalt and aggregate [53]. The substrate of the specimen was prepared using the mortar embedding method. Specifically, aggregates with a particle size of 16 mm were embedded in cement mortar. Upon hardening, the blocks were cut to expose a flat, fresh aggregate surface. Subsequently, heat-resistant acrylic rings were utilized to define the bonding area. The prepared asphalt was poured onto the surface of the aggregate, and metal pull-off stubs with a diameter of 20 mm were attached. All specimens were initially conditioned at 20°C under constant humidity for 24 h. For EA specimens, to ensure the successful completion of the cross-linking reaction, curing was conducted at 60°C for a period of 4 d. To evaluate the impact of moisture erosion on interfacial bonding performance, the specimens were categorized into dry and immersion groups. The dry group was stored at ambient temperature, whereas the immersion group was placed in a water bath at 60°C for accelerated moisture damage treatment lasting 48 h, respectively. Following the water bath, the specimens were removed and cooled for 30 min in an environment with constant temperature (20°C) and humidity to eliminate the influence of thermal stress. Testing was performed using a digital adhesion tester (Model DK500) at

503 20°C. A vertical pulling force was applied to the specimen with a loading rate strictly controlled at
504 0.7 MPa/s. Loading continued until failure occurred at the asphalt-aggregate interface, and the
505 maximum pull-off strength at failure was recorded as $P_{\text{As-Agg}}$. In addition, to evaluate the interfacial
506 moisture damage resistance, the Pull-off Strength Ratio (*PSR*) was introduced based on the corrected
507 interfacial strength. This parameter is defined as the ratio of the strength after water immersion ($P_{\text{As-}}$
508 $_{\text{Agg1}}$) to the unimmersed strength ($P_{\text{As-Agg0}}$), as expressed by Eq. (13).

509 Given the irregularity of the aggregate surface and the potential interference of the cement matrix
510 in the mortar embedding method, direct calculation of $P_{\text{As-Agg}}$ may contain errors. To obtain precise
511 interfacial strength between aggregate and asphalt, this study proposed an area normalization method
512 based on Python and Computer Vision, as shown in Fig. 10. The specific workflow is as follows: i)
513 Image annotation: Photoshop was utilized to annotate the failure interface, marking the aggregate
514 region and the non-aggregate region with specific colors (e.g., red and green). ii) Masking: A Python
515 script read the image and converted it to the HSV color space. The cv2.inRange() function was used
516 to set thresholds, creating a Binary Mask to distinguish the target region from the background. iii)
517 Processing: Morphological Closing was applied to remove noise and fill holes, ensuring the integrity
518 of the regional contours. Subsequently, cv2.findContours() was employed to extract contours and
519 calculate the actual Effective Bonding Area of the aggregate. iv) Normalization: The pull-off force
520 was normalized based on the extracted effective aggregate area. This step eliminates interference
521 from the cement matrix region in the experimental data, ensuring the accuracy and comparability of
522 bond strength indices among different specimens. Finally, the corrected interfacial strength was
523 calculated using Eq. (14).

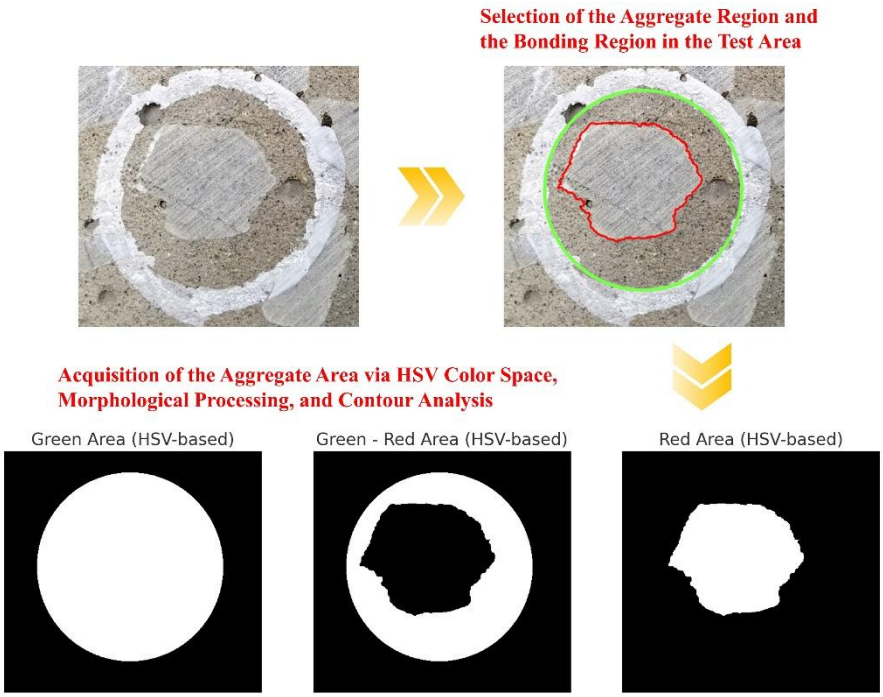


Fig. 10. Processing procedure of pull-off test data

$$PSR=\frac{P_{\text{As-Agg1}}}{P_{\text{As-Agg0}}} \tag{13}$$

$$P_{\text{As-Agg}}=\frac{P_{\text{T}\times}S_{\text{T}}-P_{\text{c}\times}S_{\text{c}}}{S_{\text{agg}}} \tag{14}$$

Where, $P_{\text{As-Agg}}$ represents the corrected interfacial strength (MPa); P_{T} denotes the interfacial strength of the aggregate group (MPa); S_{T} signifies the interfacial area of the aggregate group (px^2); P_{c} stands for the interfacial strength of the blank group (MPa); S_{c} refers to the interfacial area of the cement portion within the aggregate group (px^2); S_{gg} indicates the interfacial area of the aggregate portion within the aggregate group (px^2).

3. Results and discussion

3.1. Adhesion work of the asphalt-aggregate interface system

As illustrated in Fig. 11, the incorporation of EPS significantly enhanced the W_{adhesion} at the asphalt-aggregate interface. As the content of EPS increased from 0% (BA) to 40% (EA40), the average absolute value of W_{adhesion} across all mineral systems rose by approximately 141 mJ/m^2. In

terms of energy components, this enhancement is attributed primarily to the dominance of electrostatic interactions ($W_{Coulombic}$). Although BA is composed mainly of non-polar components and relies heavily on van der Waals forces (W_{Vander}) for adhesion, the introduction of EPS—rich in polar functional groups such as epoxy and hydroxyl groups—significantly increases the average dipole moment of the system. While this shift results in a decrease in the proportion of non-polar components and a slight reduction in W_{Vander}, it drastically strengthens the Coulombic interactions between polar groups within the asphalt and oxides on the mineral surface [54, 55]. This indicates that modification with EPS induces a fundamental transformation in the mechanism of interfacial adhesion: a shift from physical adsorption dominated by van der Waals forces to a high-strength adhesion mode governed by strong electrostatic interactions.

Due to variations in surface chemical environments and ion distributions, different mineral crystals exhibit distinct adhesion responses. In the EA40 system, the ranking of the absolute magnitude of $W_{adhesion}$ for the various mineral phases is as follows: C_2S>$CaCO_3$>C_2F>Fe_3O_4>$Ca[Al_2Si_2O_8]$>CaO>$Na[AlSi_3O_8]$>$Ca(OH)_2$. Among these, C_2S demonstrates the most superior adhesion performance, reaching an absolute $W_{adhesion}$ of 702.51 mJ/m^2 at 60°C. This is primarily derived from the extremely high electrostatic potential contribution of the surface ($W_{Coulombic}$=-695.80 mJ/m^2). Similarly, $CaCO_3$ and C_2F achieved substantial increases in strength due to epoxy modification, with absolute increments of 319.8 mJ/m^2 and 159.4 mJ/m^2, respectively. Mechanistic analysis reveals that the balanced distribution of ions on the surfaces of these minerals forms strong dipole interactions with polar groups in EA, thereby significantly amplifying the contribution of Coulombic forces.

In contrast to the active minerals mentioned above, certain minerals exhibit a weaker response to epoxy modification. For instance, the increase for CaO after modification was merely 2.38 mJ/m^2

at 25°C, while $Ca[Al_2Si_2O_8]$ displayed weak overall adhesion due to low surface chemical activity. Notably, $Ca(OH)_2$ exhibits an extremely low work of adhesion, even showing positive electrostatic potential energy in BA ($W_{Coulombic}$=26.75 mJ/m^2), which suggests the presence of electrostatic repulsion. This is attributed mainly to polarity mismatch: the surface of $Ca(OH)_2$ is rich in strongly hydrophilic -OH groups, whereas the asphalt matrix is generally hydrophobic. This disparity in polarity leads to poor interfacial wettability, making it difficult to establish effective dipole orientation and electrostatic adsorption, thus limiting the formation of interfacial strength.

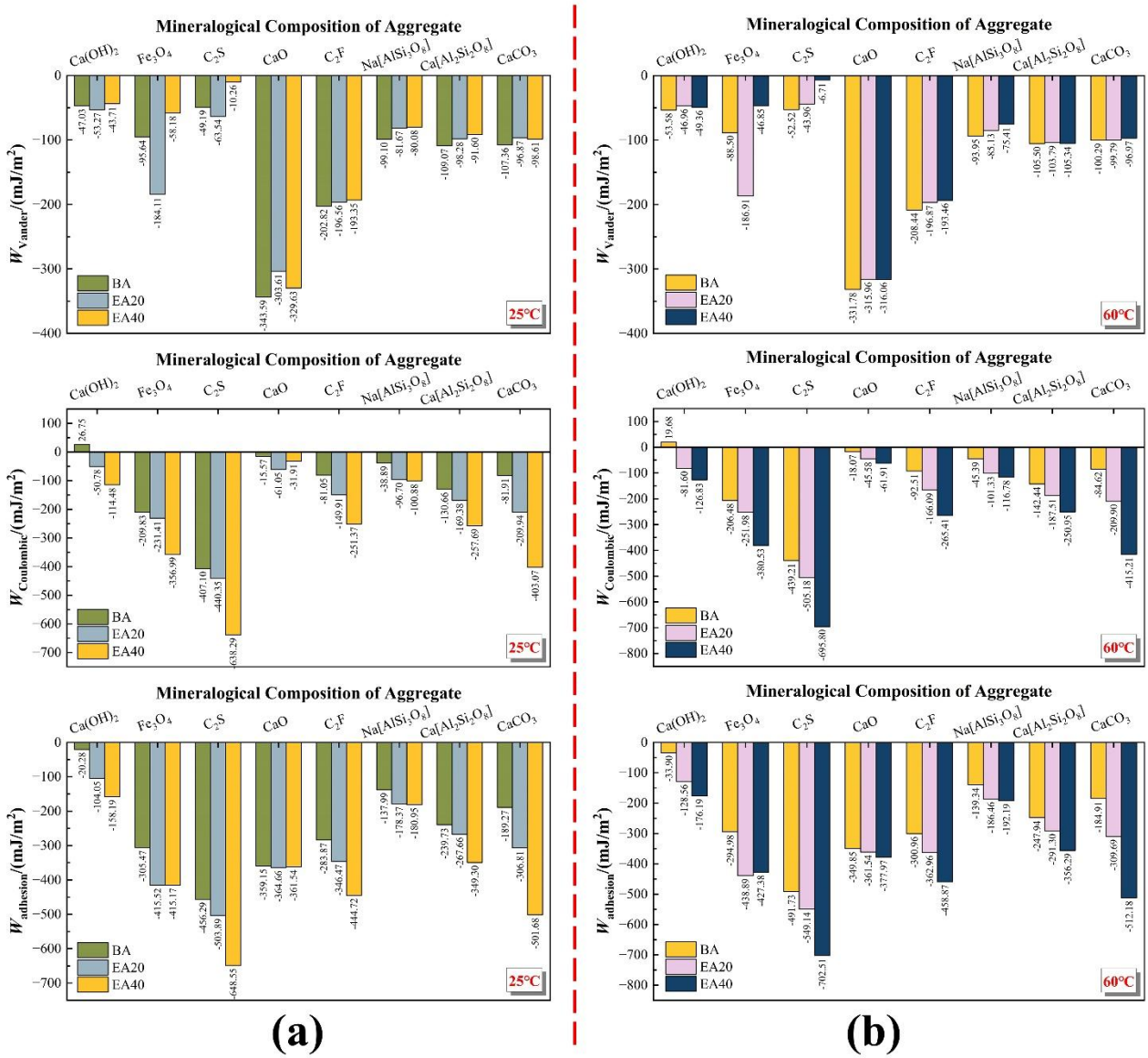


Fig. 11. Bond energy and $W_{adhesion}$ at the interface between different aggregates and asphalt: (a) 25°C; (b) 60°C

As illustrated in Fig. 12, under moisture intrusion conditions, water molecules infiltrate the asphalt-aggregate interface and tend to displace the original asphalt film. To quantitatively evaluate the interfacial stripping potential and moisture damage resistance, $W_{debonding}$ and *ER* are introduced as evaluation indices. Generally, an *ER*<1.0 indicates that moisture displacement at the interface is a thermodynamically spontaneous and severe process, making it highly prone to triggering stripping failure [56]. The results show that across all mineral systems, the *ER* exhibits a monotonically increasing trend with the increase in EPS content. Taking the $CaCO_3$ as an example, its $W_{debonding}$ is significantly reduced by the introduction of EPS. Specifically, it drops from 606.88 mJ/m^2 in the BA system to 87.59 mJ/m^2 in the EA40 system at 25°C, and further decreases from 588.80 mJ/m^2 to 74.99 mJ/m^2 at 60°C. Correspondingly, at 25°C, the *ER* increases from 0.31 for the BA system to 5.73 for the EA40 system, indicating that epoxy modification can significantly enhance wet-state interfacial stability, reduce the thermodynamic affinity of the interface for moisture, and effectively inhibit the displacement of the asphalt film by water. Notably, the *ER* of the EA40 system reaches 6.83 at 60°C, representing an increase of 2103.23% compared to the base asphalt system. Although this relative increment partially stems from the percentage amplification effect caused by the low initial *ER* of the base asphalt, its absolute value far exceeds the critical criterion of *ER*=1.0, demonstrating that epoxy modification can substantially improve the moisture stripping resistance of the interface under high-temperature conditions. Although epoxy modification generally enhances interfacial moisture damage resistance, the responses of different mineral components to moisture erosion still exhibit distinct differences. Among them, the $Ca(OH)_2$ system consistently displays the lowest *ER* under all conditions, indicating that its interface is the most sensitive to moisture displacement. This is primarily because the surface of $Ca(OH)_2$ possesses strong polarity, enabling it to form stable interactions with water molecules, thereby leading to high moisture susceptibility and

poor wet-state interfacial stability.

Although the main mineral components of steel slag generally exhibit good interfacial adhesion, the free CaO within it is prone to hydration reactions upon contact with water, generating $Ca(OH)_2$. Therefore, it is recommended to subject steel slag to a carbonation pretreatment in engineering applications, converting surface free CaO and its hydration products into stable $CaCO_3$ to reduce the moisture damage risk of the steel slag system. Furthermore, because limestone is rich in $CaCO_3$ and exhibits high interfacial stability with the epoxy asphalt system, it shows great application potential in service environments with stringent requirements for moisture damage resistance. Regarding basalt aggregates, priority can be given to mineral sources rich in $Ca[Al_2Si_2O_8]$ to fully leverage its superior interfacial moisture stripping resistance compared to $Na[AlSi_2O_6]$.

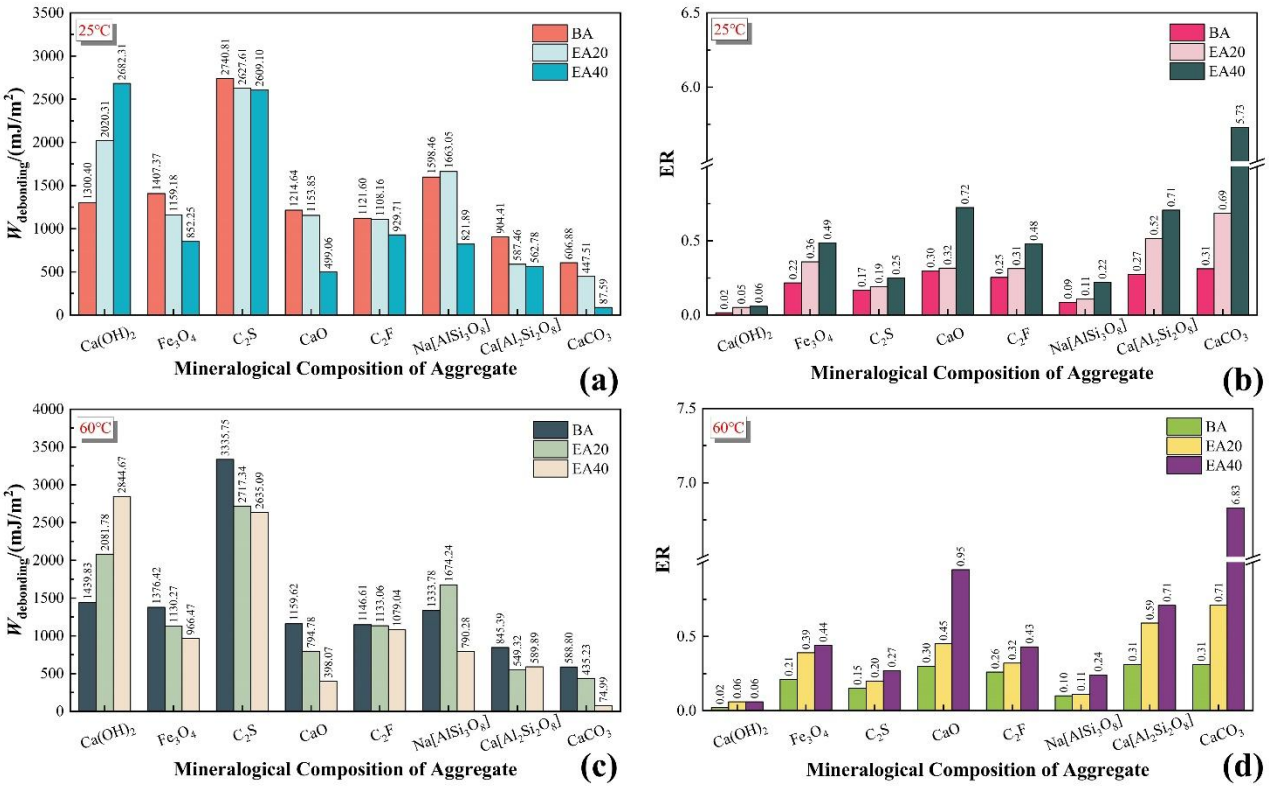


Fig. 12. Calculated results for $W_{debonding}$ and *ER* at different asphalt-aggregate interface systems: (a) $W_{debonding}$ at 25°C; (b) *ER* at 25°C; (c) $W_{debonding}$ at 60°C; (d) *ER* at 60°C

3.2. Diffusion behavior of EA within the interface system

Based on the evolution curves of *MSD* at 25°C shown in Fig. 13(a), the diffusion behavior of EA40 on the surfaces of different aggregates exhibits three typical stages: the initial adsorption stage (0–100 ps, rapid non-linear diffusion), the stable diffusion stage (100–300 ps, linear diffusion), and the later stage of anomalous diffusion. According to the Einstein relation, only the slope of the linear interval accurately reflects the characteristics of Brownian motion. Therefore, this study selected the stable interval of 150–250 ps to fit and calculate *D*. As presented in Fig. 13(b), the ranking of *D* for the various mineral surfaces is: Ca_2SiO_4<$CaCO_3$<C_2F<Fe_3O_4<$Ca[Al_2Si_2O_8]$<CaO<$Na[AlSi_3O_8]$<$Ca(OH)_2$.

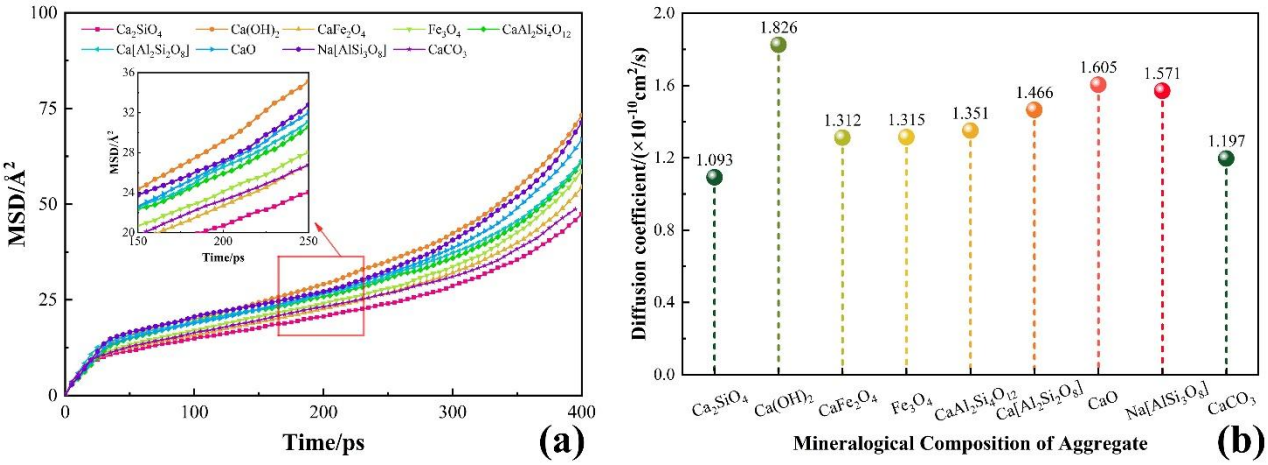


Fig. 13. (a) *MSD* of EA40 on the surfaces of various aggregate mineral components; (b) *D* of asphalt on different aggregates

A comparison between *D* and $W_{adhesion}$ reveals a significant negative correlation; specifically, stronger interfacial adhesion corresponds to a lower rate of molecular diffusion. This phenomenon is attributed to surface energy levels and mechanisms of electrostatic constraint. On one hand, surfaces rich in metal cations (Ca^{2+}, Fe^{3+}), such as C_2S and $CaCO_3$, generate intense Coulombic electrostatic attraction with polar groups within EA. These high-intensity interactions constitute energy traps that firmly anchor the macromolecular cross-linked network onto active sites. The resulting steric hindrance and kinetic confinement significantly inhibit the free migration of chain segments [49, 55].

Conversely, the interaction between asphalt and silicate minerals dominated by covalent bonds (such as $Na[AlSi_3O_8]$) relies mainly on weaker van der Waals forces. This interface with a low energy barrier imposes less restriction on molecules, allowing asphalt molecules to exhibit higher fluidity. Furthermore, $Ca(OH)_2$ possesses the highest *D*. It is hypothesized that extreme saturation of surface -OH groups leads to a poor polarity match with functional groups in EA (Polarity Saturation), failing to form effective anchors for chemical adsorption.

From an engineering perspective, the high adhesion-low diffusion response mode of mineral surfaces to EA is more favorable for the long-term durability of the interface. A lower *D* implies that interfacial molecular chains exist in a state of thermodynamic stability, forming an immobilized interface layer resistant to shearing and water displacement [57]. Although the high polarity of EA40 universally enhances wettability on all aggregate surfaces, the chemical attributes of the mineral itself remain the core factor determining interfacial dynamics. Specifically, stronger surface polarity leads to more pronounced restriction of molecular motion, thereby forming a denser and more stable interface with mechanical interlocking. In contrast, while low-polarity surfaces facilitate molecular spreading, the potential for resistance to stripping within the interfacial bond remains relatively weak.

3.3. Distribution characteristics of EA components across different interfaces

To quantify the heterogeneity of the spatial distribution of components within the EA40 system perpendicular to the surface of the aggregate (Z-axis), *RC* distribution curves were calculated, as shown in Fig. 14. Given the geometric differences among various mineral models, coordinates along the Z-axis were normalized using the top surface of the aggregate as the origin. Results indicate that adsorption of EA40 on the surfaces of different aggregates exhibits a similar Layering Phenomenon: saturates and resins with lower molecular weights display significant affinity for the interface. These components preferentially form a high-concentration primary adsorption layer (with peak

concentrations reaching 8%–10%) in the near-interface region, located 5–20 Å from the surface of the aggregate. In comparison, concentration peaks for aromatics, asphaltenes, and the epoxy cross-linked network are distributed primarily in the secondary layer. This suggests that during the process of competitive adsorption, light components with high mobility penetrate voids on the mineral surface more readily, playing a crucial role in establishing initial wetting and adhesion of the interface.

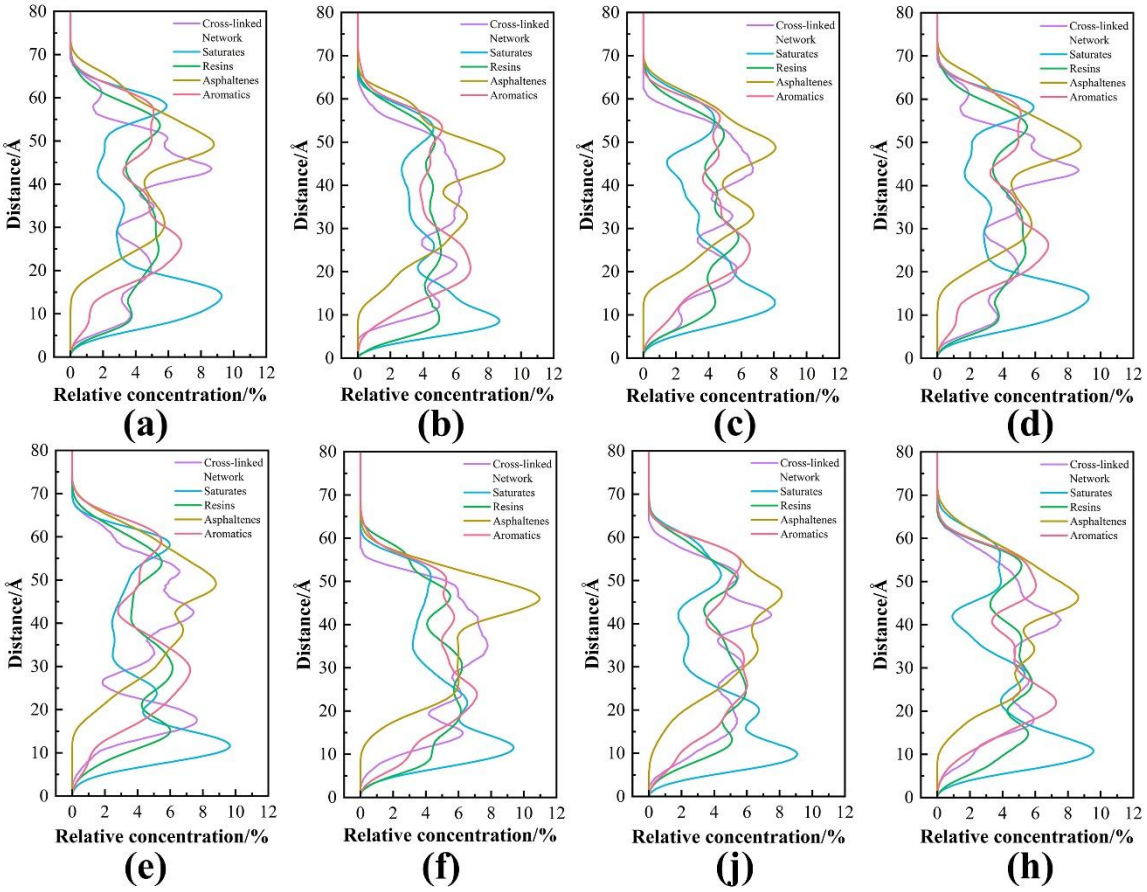
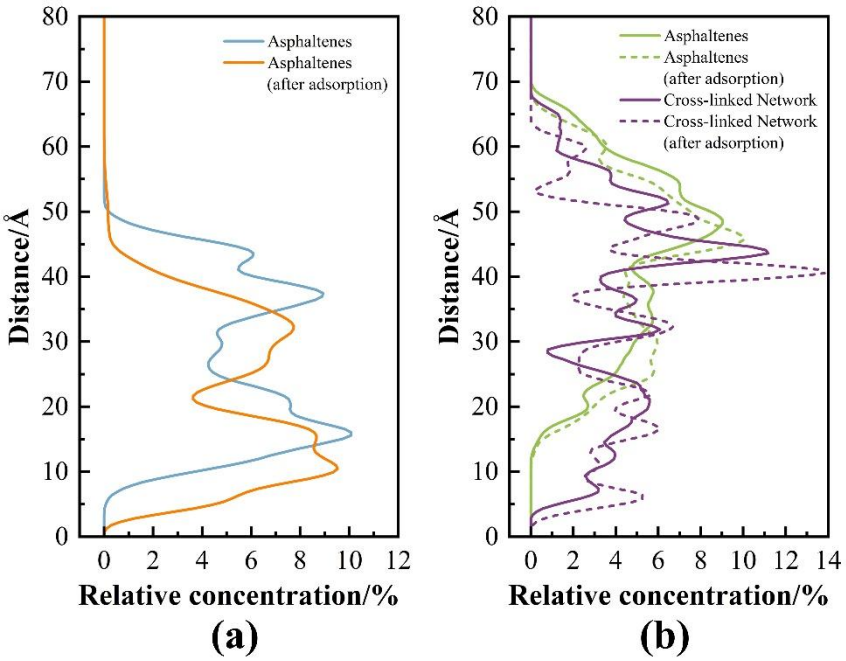


Fig. 14. Relative concentration of EA40 components along the Z-axis within interfacial systems formed by EA40 and various aggregates: (a) Fe_3O_4; (b) CaO; (c) $Ca(OH)_2$; (d) C_2F; (e) Ca_2SiO_4; (f) $Ca[Al_2Si_2O_8]$; (j) $Na[AlSi_3O_8]$; (h) $CaCO_3$;

Simultaneously, the chemical attributes of the mineral components significantly influence the compactness of the interfacial layer. Comparative analysis reveals that on active mineral surfaces rich in metal cations such as Ca^{2+} and Fe^{3+}, the relative concentration peaks for resins, saturates, and the epoxy cross-linked network exhibit higher intensity. Furthermore, the positions of these peaks are

located closer to the surface of the aggregate. This phenomenon is attributed to the synergistic effect between Coulombic electrostatic attraction and van der Waals forces. Specifically, high-energy surfaces exert a stronger traction effect on polar components, promoting the formation of a more compact and ordered packing configuration at the interface. This finding aligns with the results regarding $W_{adhesion}$ mentioned previously.

To elucidate the reconstruction mechanism of epoxy modification on the microstructure of asphalt, the spatial distribution behavior of asphaltenes in EA40 and BA was further compared, as illustrated in Fig. 15. Results indicate fundamental differences between the two. Specifically, within the BA system, asphaltene molecules tend to migrate rapidly toward the aggregate surface and accumulate there. Conversely, in the EA40 system, the migration of asphaltenes is significantly inhibited; the concentration peaks do not appear close to the interface but rather cluster between adjacent epoxy cross-linked networks. This anomalous distribution is attributed to the Steric Hindrance Effect generated by the three-dimensional network structure of the EPS. The cross-linked network establishes a physical barrier within the asphalt matrix, restricting the free diffusion and interfacial migration of heavy components (macromolecular asphaltenes). Although this network locking mechanism reduces the direct adsorption of asphaltenes at the interface to some extent, it enhances the overall cohesion and shear resistance of the system by forming a uniform Interpenetrating Network.



678

679 **Fig. 15.** Variations in relative concentration for different asphalt during the adsorption process: (a)

680 BA; (b) EA40

681 ***3.4. Micro-surface energy***

682 The results of the sessile drop test are presented in Table 8. The hydrophilicity of the different

683 aggregate surfaces differs significantly, with the contact angle of distilled water following the order:

684 limestone>basalt>SS. The minimal contact angle of SS reveals its strong hydrophilic character,

685 predicting a high risk of water wetting. Surface energy results, calculated based on contact angles,

686 are shown in Table 9. It is evident that the surface energy of the aggregates is far higher than that of

687 the asphalt, with SS exhibiting the highest surface energy (a polar component reaching 118.32 mJ/m^2).

688 This is attributed to its complex network structure of covalent and ionic bonds [58]. Regarding the

689 asphalt binders, the introduction of EPS induced a significant reconstruction of surface energy

690 components. The polar component of EA40 leaped from 0.28 mJ/m^2 to 3.82 mJ/m^2, while the

691 dispersion component increased synchronously. This dramatic surge in the polar component results

692 from the generation of abundant polar functional groups during the curing process of EPS, providing

693 a thermodynamic basis for enhanced interfacial interaction.

694 **Table 8.** Contact angle test results for the various materials

Material type	Contact angle/°		
	Distilled water	Formamide	Glycerol
BA	98.0	80.5	89.5
EA20	103.3	84.5	94.3
EA40	100.3	86.1	96.9
Basalt	51.9	23.3	75.4
Limestone	61.9	33.3	85.4
SS	45.7	24.9	78.2

695 **Table 9.** Test results for surface energy parameters of the different materials

Material type	Surface free energy/(mJ/m^2)	Polar component/(mJ/m^2)	Dispersion component/(mJ/m^2)
BA	26.55	0.28	26.27
EA20	28.39	0.94	27.45
EA40	35.02	3.82	31.20
Basalt	360.28	90.08	270.20
Limestone	412.62	91.69	320.93
SS	413.96	118.32	295.64

696 The calculation results for W_{as} under dry conditions are presented in Fig. 16(a). Increasing the
697 content of EPS significantly elevated the W_{as} of all systems, a result primarily attributed to the
698 chemical-physical synergistic enhancement mechanism. On one hand, the high polar component
699 introduced by EPS enhances the effects of the electrical double layer and instantaneous dipole
700 interactions at the interface. On the other hand, the transition of EA from a dispersed phase to a
701 continuous phase increases surface roughness, thereby expanding the effective contact area [59].
702 Regarding the influence of aggregates, SS exhibited the strongest adhesion potential (the EA40-SS
703 system reached 257.55 mJ/m^2) due to high calcium content and high surface energy, validating the

advantage of alkaline aggregates in improving the bonding performance of asphalt [60, 61].

The calculation results for W_{asw} under wet conditions are shown in Fig. 16(b). Experimental results reveal the thermodynamic trends of moisture erosion. A decrease in the absolute value of W_{asw} signifies an enhancement in the capacity for resistance to moisture damage. Epoxy modification significantly reduced the risk of debonding for all systems. Taking limestone as an example, W_{asw} improved from -20.09 mJ/m^2 for MA to -0.97 mJ/m^2 for EA40, demonstrating excellent interfacial stability. A comparison of different aggregates reveals that limestone and EA systems exhibited the lowest work of debonding (indicating the best resistance to moisture damage). This aligns with the conclusion from the MD simulation mentioned previously regarding $CaCO_3$ possessing the highest *ER*. Conversely, although SS possesses strong dry adhesion, the absolute value of its W_{asw} remains large (reaching 28.70 mJ/m^2 for the EA40 system). This corresponds to the high debonding tendency of components such as C_2S and C_2F found in the simulation. These experimental results powerfully validate the accuracy of MD simulations in predicting behavior regarding resistance to interfacial moisture damage.

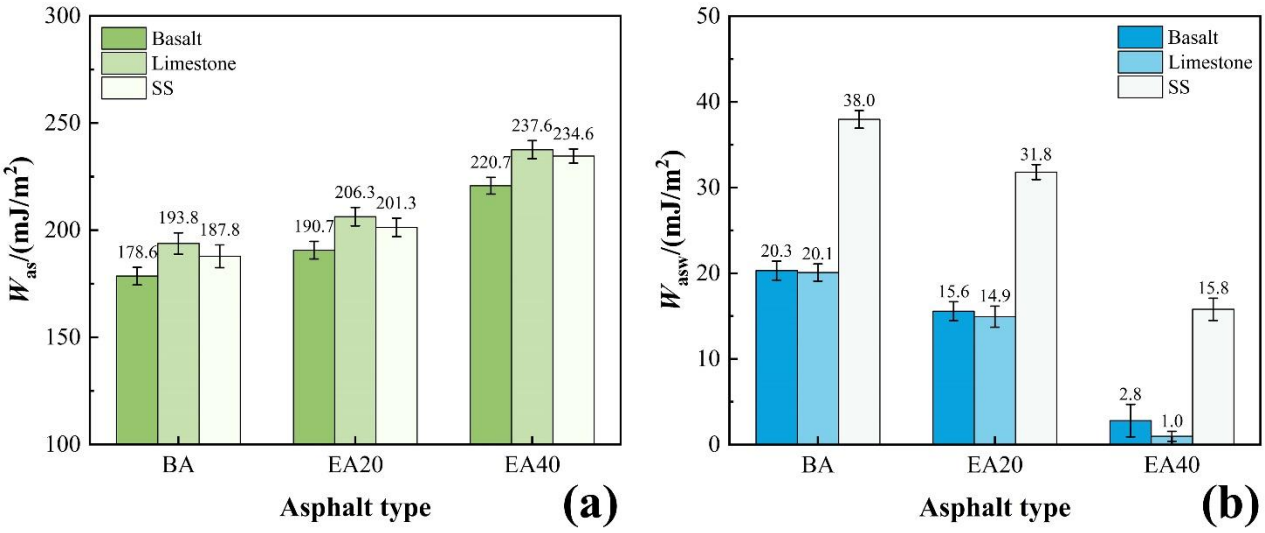


Fig. 16. Comparison of W_{as} and W_{asw} for the various samples

3.5. Adhesion strength between different aggregates and asphalt

The results of the Pull-off test are presented in Fig. 17. It is evident that the introduction of EPS produced a decisive enhancement effect on the mechanical performance of the asphalt-aggregate interface. The average adhesion strength of the BA group was maintained at approximately 2 MPa. With the increase in EPS content, the EA20 group achieved an improvement of roughly 22%, while the adhesion strength of the EA40 group generally exceeded 4 MPa. This significant leap in strength is attributed to the Interpenetrating Polymer Network formed after the curing of EPS. This network not only provides higher cohesive strength but also reinforces mechanical interlocking and chemical bonding at the interface. To quantitatively evaluate the capacity for resistance to moisture damage at the interface, the *PSR* was calculated following water bath treatment for 48 h. The results indicate that epoxy modification significantly improved the hygrothermal stability of the interface. Specifically, the *PSR* of the BA group was distributed mainly between 74% and 84%, implying a significant water displacement effect. In contrast, the *PSR* of the EA40 group jumped to a range of 91%–96%. This confirms that the EPS with a high degree of cross-linking is capable of effectively sealing interfacial pores and blocking paths of moisture intrusion, thereby maintaining extremely high interfacial integrity even in extreme hygrothermal environments.

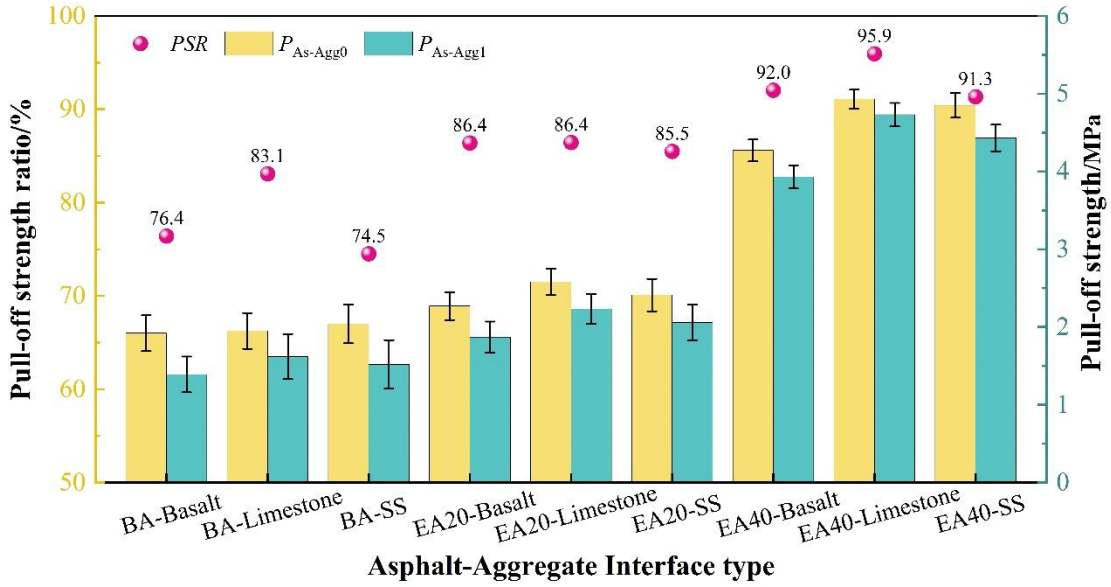


Fig. 17. Pull-off test results for different asphalt-aggregate systems

Simultaneously, the mineralogical characteristics of different aggregates resulted in differentiated bonding responses. In general, limestone exhibited the best interfacial compatibility with asphalt; particularly in the EA40 system, both its adhesion strength and *PSR* values were the highest. Although the adhesion strength of basalt was slightly lower, its *PSR* was second only to that of limestone, displaying good chemical stability. It is worth noting that while SS possessed high initial strength in the dry state, it exhibited strong sensitivity to water in the BA system. However, epoxy modification greatly overcame this defect. In the EA40-SS interface, the adhesion strength after the water bath remained as high as 4.43 MPa, and the *PSR* reached 91.34%, representing a substantial increase of 291.4% compared to the adhesion strength of the BA-SS system. This result powerfully proves that the introduction of EPS is a key technical means to solve the problem of moisture damage in SS asphalt mixtures and to fully utilize the advantage of the high mechanical strength of SS, which is consistent with the conclusions of previous experiments [9, 15].

4. Conclusions

By integrating MD simulations with laboratory tests, this study deeply analyzed the interfacial interaction behavior between EA and aggregates at the atomic scale. The work elucidated the key mechanisms by which epoxy modification enhances the moisture stability of SS asphalt mixtures. The principal conclusions are as follows:

a) In traditional asphalt systems, interfacial adhesion relies primarily on van der Waals forces. However, following epoxy modification, polar functional groups rich in epoxy and hydroxyl units significantly enhance electrostatic interactions with metal ions on the aggregate surface. This transition shifts interfacial adhesion from weak physical adsorption to a high-stability bonding mode dominated by strong electrostatic actions. Notably, high-activity mineral phases in SS, represented by C_2S and $CaCO_3$, exhibited the most optimal interfacial

response characteristics.

b) Under moisture intrusion conditions, the introduction of EPS significantly suppressed $W_{debonding}$, substantially reducing the thermodynamic driving force for moisture stripping. The significant increase in the *ER* of the EA40 system indicates that epoxy modification effectively mitigates the destructive effect of moisture on interfacial bonding, providing a molecular-level explanation for the intrinsic mechanism behind the superior moisture damage resistance of epoxy asphalt.

c) A distinct negative correlation exists between interfacial adhesion strength and the molecular diffusion coefficient. Strong interactions between high-polarity mineral surfaces and EA significantly enhance the stability of interfacial bonding. Simultaneously, the steric constraint effect generated by the cross-linked network structure further restricts the migration behavior of asphalt molecules. This facilitates the formation of a dense and stable interfacial layer structure, thereby improving the long-term service durability of the interface.

d) Light components migrate preferentially toward the aggregate surface to form an initial adsorption layer, whereas the interfacial enrichment behavior of heavy asphaltenes is markedly suppressed under the constraint of the epoxy cross-linked network. This molecular rearrangement mechanism, dominated by the cross-linked network, enhances the overall cohesion of the system while avoiding the risk of interfacial embrittlement caused by excessive accumulation of heavy components.

e) Laboratory experimental results demonstrate high consistency with the conclusions from MD simulations. The *PSR* of the EA40-SS system reached 91.34% after water bath treatment, a significant improvement over the BA system, proving that EA effectively

overcomes the water sensitivity defects of SS.

f) Future research may further introduce surface chemical reaction processes of SS, such as hydration and carbonation, alongside long-term aging factors to construct dynamic interface models closer to service conditions. Additionally, building upon the key mineral phase patterns discovered in this study, including the distinct moisture sensitivity and adhesion characteristics of C_2S and CaO, combining reactive MD or mesoscale simulation methods will deepen the investigation into the evolution mechanisms of the EA–SS system in complex environments.

Acknowledgements

This work was undertaken with funding from the Young Scientists Fund of the National Natural Science Foundation of China (Type A) (No. 52525807), the National Natural Science Foundation of China (No. 52278445), Jiangsu Provincial Natural Science Foundation Climbing Project (No. BK20250011), Jiangsu Provincial Transportation Engineering Construction Bureau Scientific Research Project (No. H202510253), and the SEU Innovation Capability Enhancement Plan for Doctoral Students (No. CXJH_SEU 24041). Moreover, the author would like to express their gratitude to the China Scholarship Council (CSC) for funding this research.

References

[1] Y. Xiong, H. Guo, D.D.M.M. Nor, A. Song, L. Dai, Mineral resources depletion, environmental degradation, and exploitation of natural resources: COVID-19 aftereffects, Resources Policy 85 (2023) 103907.

[2] C. Lu, K. Wang, Natural resource conservation outpaces and climate change: Roles of reforestation, mineral extraction, and natural resources depletion, Resources Policy 86 (2023) 104159.

[3] H. Yi, G. Xu, H. Cheng, J. Wang, Y. Wan, H. Chen, An overview of utilization of steel slag, Procedia Environmental Sciences 16 (2012) 791-801.

[4] C. Ma, S. Zhang, K. Li, T. Zhao, Q. Meng, D. Guan, A. Zhang, Stainable Utilization Strategies for Basic Oxygen Furnace Slag: Properties, Processing, and Future Directions, Metals 15(5) (2025) 537.

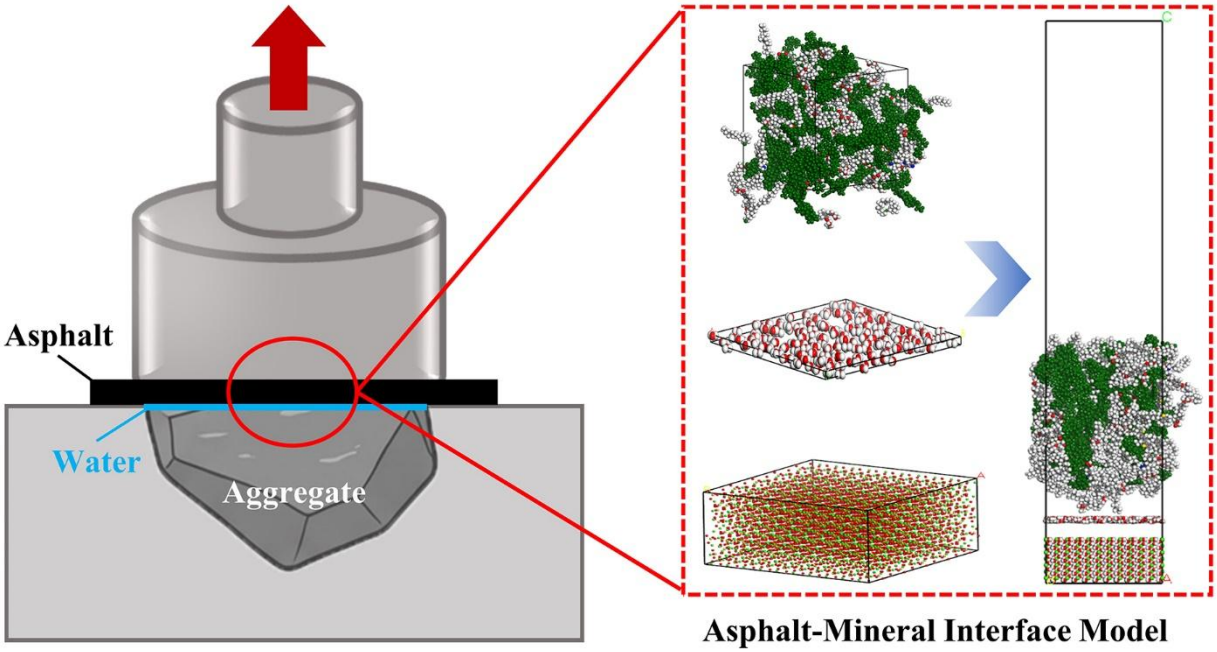
[5] J. Guo, Y. Bao, M. Wang, Steel slag in China: Treatment, recycling, and management, Waste management 78 (2018) 318-330.

[6] C. Yang, Z. Huang, S. Wu, X. He, Y. Su, Z. Zhao, H. Xu, F. Wang, L. Zhang, Recycling steel slag as aggregate in developing an ultra-thin friction course with high comprehensive road performance, Construction and Building Materials 449 (2024) 138539.
[7] W. Zhang, C. Xiao, Q. Hong, J. Liu, B. Yu, Q. Li, Z. Li, Testing and evaluation for skid resistance of steel slag asphalt wearing course based on surface texture characteristics, Construction and Building Materials 411 (2024) 134597.
[8] H. Wang, J. Qian, J. Liu, X. Nan, S. Qu, X. Li, Y. Liu, Wear resistance analysis of steel slag aggregates based on morphology characteristics, Construction and Building Materials 409 (2023) 133649.
[9] J. Sun, W. Huang, X. Wang, J. Hu, Y. Wang, Z. Zhang, S. Luo, Feasibility of pretreated steel slag for asphalt pavement application and risk assessment of hazardous substance leaching, Chemical Engineering Journal 498 (2024) 155497.
[10] X. Chen, M. Zhang, J. Yao, X. Zhang, W. Wen, J. Yin, Z. Liang, Research on water stability and moisture damage mechanism of a steel slag porous asphalt mixture, Sustainability 15(20) (2023) 14958.
[11] J. Sun, W. Huang, G. Lu, S. Luo, Y. Li, Investigation of the performance and micro-evolution mechanism of low-content thermosetting epoxy asphalt binder towards sustainable highway and bridge decks paving, Journal of Cleaner Production 384 (2023) 135588.
[12] S. Luo, J. Sun, J. Hu, S. Liu, Performance evolution mechanism of hot-mix epoxy asphalt binder and mixture based on component characteristics, Journal of Materials in Civil Engineering 34(9) (2022) 04022235.
[13] Z. Zhang, J. Sun, Z. Huang, F. Wang, M. Jia, W. Lv, J. Ye, A laboratory study of epoxy/polyurethane modified asphalt binders and mixtures suitable for flexible bridge deck pavement, Construction and Building Materials 274 (2021) 122084.
[14] J. Sun, S. Luo, W. Huang, J. Hu, S. Liu, Structural optimization of steel bridge deck pavement based on mixture performance and mechanical simulation, Construction and Building Materials 367 (2023) 130217.
[15] J. Sun, W. Huang, X. Wang, B. Zhang, Z. Zhang, A. Rahman, Y. Huang, S. Luo, Epoxy steel slag asphalt mixture: Achieving breakthrough in pavement performance and efficient waste resource utilization, Chemical Engineering Journal 520 (2025) 166262.
[16] J. Li, Z. Wang, M. Jia, Comprehensive analysis on influences of aggregate, asphalt and moisture on interfacial adhesion of aggregate-asphalt system, Journal of Adhesion Science and Technology 35(6) (2021) 641-662.
[17] G. Huang, J. Zhang, Z. Wang, F. Guo, Y. Li, L. Wang, Y. He, Z. Xu, X. Huang, Evaluation of asphalt-aggregate adhesive property and its correlation with the interaction behavior, Construction and Building Materials 374 (2023) 130909.
[18] K. Zhang, J. Yang, Y. Zhao, W. Xie, Y. Wang, Interfacial bonding property and microscopic damage mechanism of bitumen-aggregate in salt-freeze-thawing environment, Materials Today Communications 36 (2023) 106664.
[19] X. Chen, D. Ren, C. Ai, C. Yan, Research on multi-scale quantitative evaluation system for moisture damage resistance of asphalt concrete based on bonding performance, Construction and Building Materials 502 (2025) 144391.
[20] J. Sun, W. Huang, Y. Qin, Z. Zhang, A. Rahman, Y. Huang, Y. Du, S. Luo, Multiscale analysis of epoxy asphalt curing behavior based on molecular dynamics simulation and experiments, Progress in Natural Science: Materials International 35(6) (2025) 1202-1216.
[21] Z. Chen, J. Pei, R. Li, F. Xiao, Performance characteristics of asphalt materials based on molecular dynamics simulation–A review, Construction and Building Materials 189 (2018) 695-710.
[22] F. Nie, X. Su, M. Wang, X. Ma, K. Ou, J. Liu, H. Lin, Debonding of asphalt-aggregate interface under coupled moisture and temperature conditions: An atomistic study, Case Studies in Construction Materials 22 (2025) e04554.
[23] J. Fan, Y. Zhu, T. Ma, G. Xu, X. Ding, Interface interaction between high viscosity asphalt and aggregate: A multi-scale study based on experiments and molecular dynamics simulation, Fuel 357 (2024) 130045.

[24] Ministry of Transport of China, Standard test methods of bitumen and bituminous mixtures for highway engineering, China Standard Press, Beijing, 2011.
[25] Standardization Administration of China, Steel slag for road, China Standard Press, Beijing, 2009.
[26] Ministry of Transport of China, Test Methods of Aggregate for Highway Engineering, China Communications Press, Beijing, 2024.
[27] Q. Mao, M. Feng, X.Z. Jiang, Y. Ren, K.H. Luo, A.C. van Duin, Classical and reactive molecular dynamics: Principles and applications in combustion and energy systems, Progress in Energy and Combustion Science 97 (2023) 101084.
[28] R.L. Akkermans, N.A. Spenley, S.H. Robertson, COMPASS III: Automated fitting workflows and extension to ionic liquids, Molecular Simulation 47(7) (2021) 540-551.
[29] S. Zhu, L. Kong, Y. Fu, Y. Peng, Y. Chen, H. Wang, O. Jian, P. Zhao, W. Zhang, Effect of hydrophilic group substituent position on adhesion at the emulsified asphalt/aggregate interface, Construction and Building Materials 444 (2024) 137783.
[30] S. Liang, C. Liang, M. Li, H. Cui, Z. Wang, S. Wang, Investigation of nanoscale interfacial bonding properties in foamed asphalt cold recycled mixtures under chloride salt erosion, Case Studies in Construction Materials 21 (2024) e03390.
[31] Q. Wang, C. Tang, X. Li, Z. Li, M. Du, Comparison of COMPASS and PCFF in calculating mechanical behaviors of aramid fiber by means of molecular dynamics, Modelling, Measurement and Control B 86 (2017) 438-446.
[32] W. Xu, X. Qiu, S. Xiao, G. Hu, F. Wang, J. Yuan, Molecular Dynamic Investigations on the Adhesion Behaviors of Asphalt Mastic–Aggregate Interface, Materials 13(22) (2020) 5061.
[33] W. Sun, H. Wang, Moisture effect on nanostructure and adhesion energy of asphalt on aggregate surface: A molecular dynamics study, Applied Surface Science 510 (2020) 145435.
[34] J. Sun, W. Huang, Y. Qin, Z. Zhang, Z. Ling, A. Rahman, Y. Huang, S. Luo, Multi-Physical Properties of Epoxy Asphalt Under Component Variations: A Molecular Dynamics Simulation and Experimental Study, Journal of Applied Polymer Science 143(16) (2026) e70532.
[35] D.D. Li, M.L. Greenfield, Chemical compositions of improved model asphalt systems for molecular simulations, Fuel 115 (2014) 347-356.
[36] M.P. Allen, D.J. Tildesley, Computer simulation of liquids, Oxford university press2017.
[37] D.M. Beazley, P.S. Lomdahl, Large-Scale Molecular-Dynamics Simulations, Computers in Physics 11 (1997) 230.
[38] T. Christiansen, L. Wall, J. Orwant, Programming Perl: Unmatched power for text processing and scripting, " O'Reilly Media, Inc." 2012.
[39] Z. Du, X. Zhu, Y. Zhang, Diffusive dynamics and structural organization of moisture in asphaltic materials based on molecular dynamics simulation, Journal of Materials in Civil Engineering 33(1) (2021) 04020403.
[40] G. Xu, H. Wang, Molecular dynamics study of oxidative aging effect on asphalt binder properties, Fuel 188 (2017) 1-10.
[41] Y. Li, Y. Wu, K. Li, H. Lin, M. Wang, L. Zheng, C. Wu, X. Zhang, Recycling of epoxy resins with degradable structures or dynamic cross-linking networks: a review, Industrial & Engineering Chemistry Research 63(12) (2024) 5005-5027.
[42] G. Qian, D. Sun, J. Tay, Z. Lai, Hydrothermal reaction and autoclave stability of Mg bearing RO phase in steel slag, British Ceramic Transactions 101(4) (2002) 159-164.
[43] S.A. Morse, Basalts and phase diagrams, Springer 1980.
[44] Q.B. Meng, C.K. Wang, J.F. Liu, M.W. Zhang, M.M. Lu, Y. Wu, Physical and micro-structural characteristics of limestone after high temperature exposure, Bulletin of Engineering Geology and the Environment 79(3) (2020) 1259-1274.

[45] X. Chen, Y. Zhang, D. Hui, M. Chen, Z. Wu, Study of melting properties of basalt based on their mineral components, Composites Part B: Engineering 116 (2017) 53-60.
[46] X. Liu, E. Boek, W. Briels, P. Bennema, Analysis of morphology of crystals based on identification of interfacial structure, The Journal of chemical physics 103(9) (1995) 3747-3754.
[47] Z. Bjelobrk, P.M. Piaggi, T. Weber, T. Karmakar, M. Mazzotti, M. Parrinello, Naphthalene crystal shape prediction from molecular dynamics simulations, Cryst. Eng. Comm 21(21) (2019) 3280-3288.
[48] R. Wang, Y. Zhao, Influence of water molecule distribution on asphalt-aggregate interface debonding: Insights from adhesion energy and hydrogen bonding, Colloids and Surfaces A: Physicochemical and Engineering Aspects (2025) 137034.
[49] Y. Gao, Y. Zhang, F. Gu, T. Xu, H. Wang, Impact of minerals and water on bitumen-mineral adhesion and debonding behaviours using molecular dynamics simulations, Construction and Building Materials 171 (2018) 214-222.
[50] M. Xu, J. Yi, D. Feng, Y. Huang, D. Wang, Analysis of adhesive characteristics of asphalt based on atomic force microscopy and molecular dynamics simulation, ACS applied materials & interfaces 8(19) (2016) 12393-12403.
[51] L. Li, D. Qin, Z. Xu, Y. Feng, Study on strengthening mechanism of epoxy resin/rubber concrete interface by molecular dynamics simulation, Advances in Civil Engineering 2022(1) (2022) 5100758.
[52] G. Xu, H. Wang, Study of cohesion and adhesion properties of asphalt concrete with molecular dynamics simulation, Computational Materials Science 112 (2016) 161-169.
[53] American Association of State Highway and Transportation Officials, Standard Method of Test for Determining Asphalt Binder Bond Strength by Means of the Binder Bond Strength BBS Test, AASHTO, Washington, DC, 2022.
[54] Z. Min, M. Li, F. Chen, Q. Wang, W. Huang, K. Shao, The effect of photooxidation aging on the cohesion and interfacial adhesion behavior of epoxy asphalt with a composite acidic curing system based on molecular simulation, Journal of Applied Polymer Science 141(17) (2024) e55291.
[55] L. Gao, X. Ji, Y. Tan, Z. Wang, Y. Zhang, H. Kong, Molecular dynamics simulation of interfacial adhesion behavior between waterborne epoxy resin emulsified asphalt and aggregate, Composite Interfaces 30(7) (2023) 749-770.
[56] A. Bhasin, E. Masad, D. Little, R. Lytton, Limits on adhesive bond energy for improved resistance of hot-mix asphalt to moisture damage, Transportation Research Record 1970(1) (2006) 2-13.
[57] F. Pan, Z. Fan, M. Rochlani, G.C. Falla, S. Leischner, M. Oeser, H. Yu, P. Liu, Evaluation of adhesive properties of different mineral compositions in asphalt mixtures with experimental and molecular dynamics analyses, Buildings 13(5) (2023) 1207.
[58] Y. Tang, Z. Fu, F. Ma, P. Zhao, Y. Hou, X. Jiang, C. Peng, Effect of water molecular behavior on adhesion properties of asphalt-aggregate interface, Construction and Building Materials 402 (2023) 133028.
[59] J. Sun, Z. Zhang, J. Ye, H. Liu, Y. Wei, D. Zhang, X. Li, Preparation and properties of polyurethane/epoxy-resin modified asphalt binders and mixtures using a bio-based curing agent, Journal of Cleaner Production 380 (2022) 135030.
[60] G. Huang, Z. Chen, S. Wang, D. Hu, J. Zhang, J. Pei, Investigation of fracture failure and water damage behavior of asphalt mixtures and their correlation with asphalt-aggregate bonding performance, Construction and Building Materials 449 (2024) 138352.
[61] J. Sun, S. Luo, Y. Wang, Q. Dong, Z. Zhang, Pre-treatment of steel slag and its applicability in asphalt mixtures for sustainable pavements, Chemical Engineering Journal 476 (2023) 146802.

946 **TOC graphic**



947